The Planetary Science Journal, 4:76 (37pp), 2023 April https://doi.org/10.3847/PSJ/accb95

A High Spatial and Spectral Resolution Study of Jupiter's Mid-infrared Auroral Emissions and Their Response to a Solar Wind Compression

James A. Sinclair[1], Thomas K. Greathouse[2], Rohini S. Giles[2], John Lacy[3], Julianne Moses[4], Vincent Hue[2,5], Denis Grodent[6], Bertrand Bonfond[6], Chihiro Tao[7], Thibault Cavalié[8], Emma K. Dahl[1], Glenn S. Orton[1], Leigh N. Fletcher[9], and Patrick G. J. Irwin[10]

[1] Jet Propulsion Laboratory/California Institute of Technology, MS 183-601, 4800 Oak Grove Drive, Pasadena, CA 91109, USA; james.sinclair@jpl.nasa.gov
[2] Southwest Research Institute, 6220 Culebra Road, San Antonio, TX 78238, USA
[3] The University of Texas at Austin, Department of Astronomy, Austin, TX 78712, USA
[4] Space Science Institute, 4765 Walnut Street, Suite B, Boulder, CO 80301, USA
[5] Aix-Marseille Université, CNRS, CNES, Institut Origines, LAM, Marseille, France
[6] Université de Liège, STAR Institute, Laboratoire de Physique Atmosphérique et Planétaire, Quartier Agora allée du six Août 19 c B-4000 Liège 1, Belgium
[7] National Institute of Information and Communications Technology, 4-2-1, Nukui-Kitamachi, Koganei, Tokyo 184-8795, Japan
[8] Laboratoire d'Astrophysique de Bordeaux, All. Geoffroy Saint-Hilaire, F-33600 Pessac, France
[9] School of Physics & Astronomy, University of Leicester, University Road, Leicester, LE1 7RH, UK
[10] Atmospheric, Oceanic & Planetary Physics, University of Oxford, Parks Road, Oxford, OX1 3PU, UK
Received 2023 February 7; revised 2023 March 23; accepted 2023 April 7; published 2023 April 27

Abstract

We present mid-infrared spectroscopy of Jupiter's mid-to-high latitudes using the Gemini-North/Texas Echelon Cross Echelle Spectrograph on 2017 March 17–19. These observations capture Jupiter's hydrocarbon auroral emissions before, during, and after the arrival of a solar wind compression on March 18, which highlights the coupling between the polar stratosphere and external space environment. In comparing observations on March 17 and 19, we observe a brightening of the CH_4, C_2H_2, and C_2H_4 emission in regions spatially coincident with the northern duskside main auroral emission (MAE). In inverting the spectra to derive atmospheric information, we determine that the duskside brightening results from upper stratospheric ($p < 0.1$ mbar/$z > 200$ km) heating (e.g., $\Delta T = 9.1 \pm 2.1$ K at 9 μbar at 67°.5N, 162°.5W) with negligible heating at deeper pressures. Our interpretation is that the arrival of the solar wind enhancement drove magnetospheric dynamics through compression and/or viscous interactions on the flank. These dynamics accelerated currents and/or generated higher Poynting fluxes, which ultimately warmed the atmosphere through Joule heating and ion-neutral collisions. Poleward of the southern MAE, temperature retrievals demonstrate that auroral-related heating penetrates as deep as the 10 mbar level, in contrast to poleward of the northern MAE, where heating is only observed as deep as ~3 mbar. We suggest that this results from the south having higher Pedersen conductivities and therefore stronger currents and acceleration of the neutrals, as well as the poleward heating overlapping with the apex of Jupiter's circulation, thereby inhibiting efficient horizontal mixing/advection.

Unified Astronomy Thesaurus concepts: Aurorae (2192); Planetary magnetospheres (997); Infrared astronomy (786); High resolution spectroscopy (2096); Aeronomy (22); Jupiter (873); Planetary atmospheres (1244); Planetary polar regions (1251)

1. Introduction

Jupiter has the largest planetary magnetosphere in our solar system. This is further augmented by volcanic emissions from Io, which load the magnetosphere with sulfur and oxygen ions and modulate magnetospheric dynamics (e.g., Bonfond et al. 2012; Yoshikawa et al. 2017). These dynamics, as well as interactions of the magnetosphere with the solar wind, ultimately drive ions and electrons into Jupiter's polar atmosphere. Precipitating particles deposit their energies at high southern and northern latitudes and ultimately produce auroral emissions over a large range of wavelengths, including the X-ray (e.g., Gladstone et al. 2002; Dunn et al. 2017; Mori et al. 2022), ultraviolet (e.g., Nichols et al. 2017; Grodent et al. 2018; Greathouse et al. 2021; Hue et al. 2021), near-infrared (e.g., Moore et al. 2017; Johnson et al. 2018), and mid-infrared (e.g., Caldwell et al. 1980; Livengood et al. 1993).

Jupiter's auroral regions are divided into three main subregions based on the morphology of the ultraviolet emissions. First, the main auroral oval or main auroral emission (MAE) is a persistent strip of emission around the magnetic poles and is thought to be generated by the breakdown of corotation in the middle magnetosphere (e.g., Grodent 2015). Second, discrete spots or "footprints" of emission, which are slightly equatorward of the MAE, result from the electromagnetic interactions of Io, Europa, and Ganymede with the rotating magnetospheric plasma (e.g., Bonfond et al. 2012). Third, the diffuse and highly variable "polar" emissions are enclosed or poleward of the MAE. These are considered to be driven by outer magnetospheric dynamics related to the Vasilyunas and Dungey cycles (e.g., Cowley et al. 2003). Jupiter's stratospheric hydrocarbon species, including CH_4, C_2H_2, C_2H_4, and C_6H_6, exhibit enhanced, mid-infrared emissions that are generally coincident with the ultraviolet polar emissions described above (e.g., Kim et al. 1985; Drossart et al. 1993; Kostiuk et al. 1993; Flasar et al. 2004). One component of the enhanced mid-infrared emissions results from heating of the atmosphere at microbar pressures (e.g.,

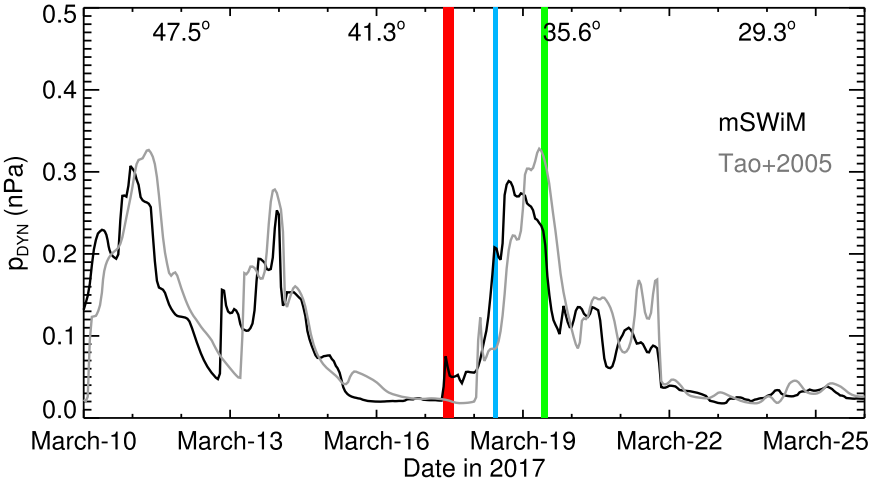

Figure 1. Predicted solar wind dynamical pressures at Jupiter in 2017 March using OMNI-measured conditions at Earth (Thatcher & Müller 2011) and two solar wind propagation models—mSWiM (Zieger & Hansen 2008) in black and the Tao et al. (2005) model in gray—to calculate the solar wind flow at Jupiter's orbit. Dates/times are UTC. Red, blue, and green lines denote the time periods on March 17, 18, and 19, respectively, where the Gemini-TEXES spectra presented in this study were recorded. The Earth–Jupiter–Sun angles are shown near the top of the panel.

Sinclair et al. 2017b, 2020) at similar altitudes as those inferred for the ultraviolet emissions and therefore presumably driven by processes such as chemical heating, H_2 dissociation from excited states, and Joule heating from Pedersen currents (e.g., Grodent et al. 2001; Yates et al. 2014; Badman et al. 2015). A second component is the enrichment of the aforementioned hydrocarbon species by higher rates of ion-neutral and electron-recombination reactions due to the influx of ions and electrons (e.g., Sinclair et al. 2017a, 2018, 2019a). A third component is a discrete layer of lower stratospheric auroral-related heating (∼1 mbar), which we consider driven by different mechanisms compared to that in the upper stratosphere. A recent analysis of Atacama Large Millimeter/submillimeter Array (ALMA) observations demonstrated the presence of eastward and westward jets at ∼0.1 mbar, horizontally coincident with the southern MAE and possibly generated by ion-neutral collisions (Cavalié et al. 2021). They suggest that the jets highlight the presence of a counterrotating vortex with the enclosed atmospheric subsidence heating the lower stratosphere through adiabatic compression. Such a vortex would confine aurorally heated and hydrocarbon-enriched gas to the region until advected to deeper pressures, where the vortex dissipates. This describes an extreme example of space weather where the magnetosphere and solar wind can modulate the thermal structure, chemistry, and dynamics as deep as the middle atmosphere.

In Sinclair et al. (2019b), a series of Subaru Cooled Mid-Infrared Camera and Spectrograph (COMICS; Kataza et al. 2000) broadband 7.8 μm images of Jupiter's CH_4 emission were presented. In comparing images recorded on 2017 January 11, 12, and 14, a brightening and subsequent dimming of the south polar emissions was observed. Images recorded on January 12 demonstrated a brightening of the CH_4 emission in a region that was spatially coincident with the duskside MAE. This duskside feature was absent ∼19 hr later, which suggested that it was also transient and presumably driven by the same mechanism driving the variable southern poleward CH_4 emissions. The arrival of a solar wind compression early on January 12 (though with a potential ∼48 hr uncertainty) was predicted using OMNI measurements of solar wind conditions at Earth (e.g., Thatcher & Müller 2011) and a one-dimensional solar wind propagation model (Tao et al. 2005) to calculate the flow out to Jupiter's orbit. The interpretation was that the solar wind compression perturbed the Jovian magnetosphere through either magnetic reconnection (e.g., Masters et al. 2021) and/or velocity shears on the nightside magnetospheric flank (e.g., Zhang et al. 2018). This ultimately accelerated energetic particles into the atmosphere, which deposited their energy in such a way as to produce (1) heating of the atmosphere, (2) vertical winds that advect CH_4 and its photochemical by-products to higher altitudes, and/or (3) excitement of CH_4 to higher rovibrational states, thereby enhancing the 7.8 μm CH_4 emissions. The daily timescales over which the variability was observed implied that these changes occurred at the highest altitudes (10–1 μbar) sensed by Jupiter's 7.8 μm CH_4 emission, where the thermal inertia timescales are shortest.

In this work, we present evidence of a similar event where the duskside mid-infrared MAEs brighten seemingly in response to the arrival of a solar wind compression. However, the observations and analysis presented in this work provide several advantages over those presented in Sinclair et al. (2019b) and allow this phenomenon to be studied with less ambiguity and greater detail. First, the observations presented in this work were recorded when Jupiter was within 50° of opposition, when the uncertainties on the magnitude and timing of the solar wind propagation results were smaller. Solar wind propagation models, such as the Michigan Solar Wind Model (mSWiM; Zieger & Hansen 2008) and a similar model first presented in Tao et al. (2005), adopt empirical solar wind conditions at Earth and use a one-dimensional magnetohydrodynamic calculation to model the solar wind flow out to the orbit of the target planet. Given variations in solar wind flow as a function of heliocentric longitude, the model results are most accurate when the target planet is close to opposition (i.e., the Sun–target–Earth angle is small). Zieger & Hansen (2008) quantified the uncertainty on the predicted solar wind conditions as a function of angle from opposition and found the uncertainties on the solar wind conditions to be <20 hr in timing and <38% in dynamical pressure when Jupiter was within 50° of opposition. Figure 1 shows predicted solar wind pressures at Jupiter during the period of observations presented in this work. A solar wind compression arrived at Jupiter's

magnetosphere on 2017 March 18. Even with a timing uncertainty as high as 20 hr, we can still confidently interpret observations recorded on 2017 March 17, 18, and 19 as having captured Jupiter's high latitudes before, during, and after the arrival of this solar wind compression. In contrast, the data presented in Sinclair et al. (2019b) were recorded when Jupiter was ∼80° from opposition, where uncertainty could be as high as 48 hr (Zieger & Hansen 2008). This introduced ambiguity into the timing of the solar wind compression arrival with respect to the observed mid-infrared MAE brightening. Second, in this work, we present high-resolution spectroscopy ($65{,}000 < R < 80{,}000$) in discrete 5–7 cm^{-1} wide bands that capture Jupiter's H_2 S(1), CH_4, C_2H_2, C_2H_4, and C_2H_6 emission features. Further details of the observations are discussed in Section 2. This allows the variability of CH_4 emission, as well as its photochemical by-products, to be measured, which can better disentangle whether any observed brightening results from a heating and/or chemistry effect. The high spectral resolution resolves individual strong and weak emission lines of the aforementioned hydrocarbons, which in turn sounds a large range of altitudes in Jupiter's stratosphere and mesosphere (Section 3.3). By inverting these spectra using radiative transfer software, changes in atmospheric temperatures and/or abundances can be quantified and the altitudes at which they occur better determined. In contrast, the data presented in Sinclair et al. (2019b) were broadband ($\Delta\lambda \sim 0.7\ \mu$m) 7.8 μm imaging of Jupiter's CH_4 emission, which did not allow retrieval of atmospheric information without significant degeneracy.

2. Observations

High-resolution spectra were recorded using the Texas Echelon Cross Echelle Spectrograph (TEXES; Lacy et al. 2002) on the 8 m Gemini-North telescope on 2017 March 17–19. Spectra were recorded in discrete settings centered at 587, 730, 819, 950, and 1248 cm^{-1}, which respectively capture stratospheric $H_2S(1)$ quadrupole, C_2H_2, C_2H_6, C_2H_4, and CH_4 emissions. These observations were performed when the relative Earth–Jupiter velocity was 10–12 $km\,s^{-1}$, which produces a Doppler shift sufficient to disentangle Jovian CH_4 emission lines from telluric CH_4 absorption.

The $4'' \times 0\farcs5$ slit of the spectrograph was aligned parallel to the direction of Jupiter's central meridian. Starting from dark sky west of the planet, the slit was stepped across Jupiter's high northern latitudes in steps of a half slit width for Nyquist sampling until the slit reached four planet-free steps east of the limb. Successive scans were repeated with the slit offset in a direction parallel to Jupiter's central meridian in order to build up latitudinal coverage. The same process was repeated at Jupiter's high southern latitudes. Looping through the five aforementioned spectral settings, scans of both high southern and high northern latitudes were repeated over the course of each night with Jupiter's rotation used to build up longitudinal coverage. For the 587 cm^{-1} spectral setting, a wider, $0\farcs8$ slit was used due to the larger angular diffraction at longer wavelengths. Further details of individual scans are provided in Table A1.

Sky emission sampled at the start and end of each scan allowed for subtraction of sky emission from the measured spectra of the target. The wavelength-dependent absolute calibration for each spectrum was performed using corresponding exposures of a blackbody card of known temperature mounted above the instrument's window. Custom IDL software and the Navigation and Ancillary Information Facility SPICY toolkit (Acton 1996) were used perform a limb-fitting procedure in order to calculate the latitude, longitude, emission angle, and velocity (combining Jupiter's radial and rotational velocity) of each pixel. In this work, we use planetocentric latitude and the System III longitude system. Each individual spectrum was corrected for Doppler shift. Figures B1–B10 show the distributions of individual observations sorted by setting, hemisphere, and chronological order, with each spectrum colored according to the radiance of an emission line of the relevant species.

From these individual scans alone, we noticed significant variability in the strength and morphology of the hydrocarbon emissions within the main ovals over the 3 days of observations. For example, on March 17, observations of the northern oval in scans 7017.01, 7018.01, and 7018.02 show a single hot spot of the strongest CH_4 emissions at a longitude of approximately 180°W, whereas 2 days later, observations in scans 9011.01 and 9011.02 show that the strongest CH_4 emissions are in two distinct regions, the first on the eastern or duskside of the main oval and the second at longitudes of approximately 190°W–200°W (Figure B9). Similar changes in morphology inside the northern main oval between March 17 and 19 are also evident in the 730 cm^{-1} spectra of the C_2H_2 emission (Figure B3). Two regions of stronger C_2H_4 emissions within the northern main oval are also evident in the 950 cm^{-1} observations recorded on 2017 March 19 (see Figure B7). Although the same regions were not sufficiently sampled at 950 cm^{-1} on March 17 to indicate whether this morphology is transient, the fact that a similar morphology is observed in the CH_4 and C_2H_2 emissions strongly suggests that the C_2H_4 features are also transient features that emerged sometime between 2017 March 17 and 19.

In the south, we also observe the variability of the poleward emissions between dates. For example, C_2H_2 emission poleward of the main auroral oval decreases from March 17 (see scans 7044.01 and 7044.02; Figure B4) to 18. A similar marginal decrease of the C_2H_6 emissions is also observed between March 17 and 18 (Figure B6), whereas an increase in C_2H_4 emissions is observed between March 17 and 18 (Figure B8). For the CH_4 emissions, our observations did not sufficiently sample the same regions on both nights to determine whether any similar variability occurred. This possibly suggests that the southern poleward hydrocarbon emissions exhibit variability on timescales of hours.

In previous studies using similar TEXES spectra (e.g., Fletcher et al. 2016, 2020; Melin et al. 2018; Sinclair et al. 2018, 2020), all individual spectra recorded on 1 night or across several nights were combined to extend longitudinal coverage and then coadded into latitude–longitude bins to increase the signal-to-noise ratio for the radiative transfer analysis. Given the longitudinal overlap between scans and the temporal variability of the hydrocarbon emissions evident in the northern main oval, we chose to coadd only a subset of the scans such that temporal variability was not diluted or averaged out entirely. The scans chosen for coaddition and further analysis are shown in bold in Table A1. For observations on March 17 and 19, we coadded spectra only at high northern latitudes to focus on the variability of the northern auroral oval between these dates. At high southern latitudes, spectra on March 17 and 19 did not sufficiently sample the same locations

in all five spectral settings. Similarly, for observations on March 18, we coadded observations only at high southern latitudes, since they did not sufficiently sample the northern auroral oval. Our analysis therefore only provides a snapshot of the southern auroral oval, but we note to readers that we do observe evidence of variability in the southern poleward emissions between March 17 and 18. Individual spectra were coadded into 5° × 5° latitude–longitude bins, stepped in increments of 2°.5 for Nyquist sampling. Here ∼5° corresponds to the diffraction-limited spatial resolution in latitude–longitude at 60° and the expected accuracy of the spatial registration of the spectra. Figure 2 shows the distributions of coadded observations at high southern latitudes on 2017 March 18. Figure 3 shows the distributions of coadded observations at high northern latitudes on 2017 March 17 and 19, which further highlight the variability of the hydrocarbon emissions over ∼2 days.

3. Radiative Transfer Model

The NEMESIS radiative transfer model (Irwin et al. 2008) was adopted for all forward modeling and retrievals of atmospheric information. NEMESIS assumes local thermodynamic equilibrium (LTE) and adopts the optimal estimation technique, where an initial guess or a priori, $\boldsymbol{x_a}$, of an atmospheric parameter (e.g., the vertical temperature profile) is initially adopted. A synthetic spectrum, $\boldsymbol{F}(\hat{x})$, is computed; the cost function (ϕ; Equation (1)) is evaluated; and the variable parameter, $\boldsymbol{x}$, is iteratively adjusted until it converges on a solution that minimizes the cost function (Equation (1)),

$$\phi = (\boldsymbol{y} - \boldsymbol{F}(\hat{x}))^T \boldsymbol{S_\epsilon}^{-1} (\boldsymbol{y} - \boldsymbol{F}(\hat{x})) + (\hat{\boldsymbol{x}} - \boldsymbol{x_a})^T \boldsymbol{S_a}^{-1} (\hat{\boldsymbol{x}} - \boldsymbol{x_a}). \quad (1)$$

Here $\boldsymbol{y}$ and $\boldsymbol{S_\epsilon}$ are the observed spectrum and uncertainty on the observed spectrum, respectively, and $\hat{\boldsymbol{x}}$ and $\boldsymbol{S_a}$ are the retrieved value and a priori error, respectively.

3.1. Spectroscopic Line Data

We chose to perform forward modeling and retrievals using the correlated-k treatment (e.g., Lacis & Oinas 1991) of spectroscopic line data for computational efficiency. The spectroscopic line data for the H_2 S(1) quadrupole line feature, NH_3, PH_3, CH_4, CH_3D, $^{13}CH_4$, C_2H_2, C_2H_4, and C_2H_6, in Fletcher et al. (2018) were adopted in this work. The k-distributions for the aforementioned species were calculated from 728–733, 815–824, 947–953, and 1244–1252 cm^{-1} using a 4 $km\,s^{-1}$ sinc-squared convolution. Due to the effects of diffraction, a wider slit was used for the 587 cm^{-1} observations compared to the other wavelength settings. Modeling of this observation required a 6 $km\,s^{-1}$ sinc-squared convolution.

3.2. Atmospheric Model

For the vertical temperature profile, we assumed the profile adopted in Moses & Poppe (2017), which uses Short Wave Spectrometer on the Infrared Space Observatory results (Lellouch et al. 2001 and references therein) at pressures greater than 1 mbar and Galileo Atmospheric Structure Instrument measurements (Seiff et al. 1998) at pressures lower than 1 mbar. For the vertical profiles of all hydrocarbons, we adopted "Model 7" presented in Sinclair et al. (2020) but recalculated at a latitude of 60°N. These profiles were derived from a photochemical model similar to that described in Moses & Poppe (2017), except for the adoption of a larger vertical gradient in the eddy diffusion coefficient such that the CH_4 homopause resides at 7 nbar. In Sinclair et al. (2020), a 7 nbar homopause pressure was found to be the best-fitting model to observations of H_2 S(1), CH_4, and CH_3 emission inside Jupiter's northern main oval. Figure 4 shows the vertical profiles of temperature, CH_4, and its isotopologues, C_2H_2, C_2H_4, and C_2H_6, from Model 7, which we adopted in this work. The vertical profiles of temperature, C_2H_2, C_2H_4, and C_2H_6 serve as initial guess or a priori profiles in performing inversions or retrievals in Sections 4 and 5.

The vertical profiles of H_2, He, NH_3, and PH_3 were adopted from Sinclair et al. (2018). For tropospheric aerosols, we assumed a 0.7 bar NH_3 ice cloud with a 10 μm optical depth of 0.5 and fractional scale height of 0.5 and a 4.0 bar NH_4SH cloud with a 10 μm optical depth of 1.0 and a fractional scale height of 0.05. Although the physical properties of clouds and concentrations of disequilibrium species vary with latitude and longitude on Jupiter (e.g., Fletcher et al. 2016; Giles et al. 2017; Blain et al. 2018), such spatial variations modulate only the tropospheric continuum at the wavelengths presented in this work and have a negligible effect on retrieved stratospheric properties.

3.3. Vertical Sensitivity

Adopting the model atmosphere described in Section 3.2, the vertical functional derivatives with respect to temperature were calculated over the ranges of the five spectral settings. The vertical functional derivatives with respect to temperature, or contribution functions, quantify the contribution of each atmospheric level to the total observed radiance at the top of the atmosphere at a given wavelength and therefore also quantify the range of pressures/altitudes over which the observations sound.

In each spectral setting, the functional derivatives were computed and then convolved with a telluric transmission spectrum Doppler shifted by +11 $km\,s^{-1}$ to simulate Jupiter's radial velocity from −12 to −10 $km\,s^{-1}$ at the time of the observations (see Table A1). The telluric transmission spectra were calculated using ATRAN (Lord 1992) assuming an altitude of 13,800 ft (the altitude of Maunakea), precipitable water vapor of 1 mm, and an airmass of 1.4 (or zenith angle of 45°). Figure 5 shows the resulting vertical functional derivatives. In the 587 cm^{-1} spectral setting, the continuum sounds the upper troposphere at ∼100 mbar, and the H_2 S(1) quadrupole line sounds the lower stratosphere from ∼50 to ∼1 mbar. The CH_4 emission lines sampled in the 1248 cm^{-1} setting sound the atmosphere from ∼20 mbar to 0.1 μbar. As in previous studies, we invert the spectra in 587 and 1248 cm^{-1} simultaneously in order to constrain the vertical temperature profile at ∼100 mbar and from ∼50 mbar to 0.1 μbar.

In the 730 cm^{-1} setting, a mixture of weak and strong C_2H_2 emission lines sounds the atmosphere from ∼50 mbar to ∼1 μbar. The C_2H_4 emission lines measured in the 950 cm^{-1} setting exhibit a double-peaked contribution function with sensitivity peaking at approximately 1 mbar and 0.5 μbar. In the 819 cm^{-1} setting, C_2H_6 emission sounds the atmosphere from ∼20 to ∼0.08 mbar. The vertical sensitivities to the C_2 hydrocarbons differ, and we discuss the impact this has on the analysis in Section 5.

4. Temperature Results

The vertical temperature profile was retrieved by simultaneously inverting the H_2 S(1) quadrupole emission line and surrounding continuum in the 587 cm^{-1} setting and CH_4 emission in the 1248 cm^{-1} setting. The vertical profile of temperature shown in Figure 4 was adopted as the a priori profile.

4.1. High Southern Latitudes

Figure 6 shows retrieved temperature distributions at high southern latitudes using observations recorded on 2017 March 18 and demonstrates that heating associated with auroral processes is observed predominantly at longitudes inside the southern auroral oval (e.g., Sinclair et al. 2017b, 2018). In comparison to longitudes outside the southern auroral oval, temperatures are elevated at pressures as deep as ~10 mbar. This is also demonstrated in Figure 7, which compares the observed and modeled spectra and retrieved vertical profiles of temperature at 72°.5S, 300°W (equatorward of the MAE) and 32°.5W (poleward of the MAE). Auroral-related heating as deep as 10 mbar is in contrast to the results of Jupiter's northern auroral region (Section 4.2; Sinclair et al. 2017a, 2018, 2020), where no significant auroral-related heating was observed at pressures higher than 2–3 mbar. Either heating as deep as 10 mbar is a persistent feature of the southern auroral region that was not observed in previous IRTF-TEXES observations due to the poorer spatial resolution insufficiently sampling such high latitudes, or the deeper extent of heating is a transient response to the arrival of the solar wind compression. We favor the former explanation as detailed further in Section 6.

The retrieved temperature profile inside the auroral region exhibits a local maximum at ~1 mbar, which is approximately 25 K warmer than temperatures derived outside the auroral oval, where no such maximum in temperature is observed. Temperatures inside the auroral oval decrease from ~1 to 0.1 mbar, then continue to rise toward lower pressures. At pressures lower than 0.1 mbar, atmospheric heating is inferred to result from processes directly related to the deposition of energy from the magnetosphere and external space environment, including chemical heating, H_2 dissociation from excited states (Grodent et al. 2001), Joule heating from Pedersen currents (e.g., Badman et al. 2015), and ion drag. These processes essentially move the base of the thermosphere to lower altitudes, as has been shown using general circulation modeling of Jupiter's thermosphere (Bougher et al. 2005). A localized maximum in temperature at ~1 mbar has been observed in previous work using different data sets and appears to be a persistent feature of both the northern and southern auroral regions (Kostiuk et al. 2016; Sinclair et al. 2017a, 2017b, 2018, 2020). In earlier studies, we suggested that this heating resulted from shortwave solar heating of haze particles produced by the complex chemistry prevalent in Jupiter's auroral regions (e.g., Friedson et al. 2002; Wong et al. 2003). However, temperatures inside the northern auroral region at 1 mbar have been observed to vary erratically on timescales of weeks to months (Sinclair et al. 2018), which cannot be explained by longer-term variations in solar insolation. We also considered pumping of the CH_4 3 μm band by overlapping H_3^+ emission lines from higher in the atmosphere. This would, in turn, affect the transitions responsible for the 8 μm band, a component of which originates from the ~1 mbar level. However, we have also ruled this out as a dominant mechanism, since the strongest H_3^+ emissions are spatially coincident with the MAE, whereas the strongest 1 mbar heating is generally observed to be coincident with the poleward emissions. We also consider it very unlikely that the 1 mbar heating is driven directly by precipitation of magnetospheric electrons and ions. For example, Gustin et al. (2016) demonstrated that electrons do not precipitate deeper than ~200 km/0.1 mbar. Similarly, precipitation of ions, and the resulting secondary electrons, is not expected at pressures higher than ~200 km/0.1 mbar (e.g., Ozak et al. 2013; Houston et al. 2020). Instead, we favor the explanation presented in Cavalié et al. (2021), who observed anticyclonic rotation at ~0.1 mbar inside the auroral ovals, which implies the presence of atmospheric subsidence and adiabatic heating. We discuss this further in Section 6.

4.2. High Northern Latitudes

Figure 8 shows retrieved temperature distributions at high northern latitudes using observations on 2017 March 17 and 19. As for the southern auroral region, temperatures are predominantly elevated at ~1 mbar and pressures lower than 0.1 mbar. As noted previously, we observe no significant heating at pressures higher than 2–3 mbar, in contrast to what is observed of the southern auroral region. In comparing the results on March 17 and 19, morphological changes in the temperature field are apparent. On March 17, the warmest temperatures are in a single region centered at ~183°W, whereas on March 19, this region and an additional region of warm temperatures at ~162°.5W (the duskside of the northern auroral oval) are apparent. This is demonstrated further in Figure 9, which shows longitudinal cross sections of temperature at 67°.5N on March 17 and 19 and their difference.

The western region of heating extends from approximately 185°W to 200°W with ~5 K heating at the 1 mbar level and ~9 K heating at the 0.01 mbar level. This results from an (apparent) eastward shift of a region of warmer temperatures. On March 17, 0.01 mbar temperatures at 67°.5N peak at a longitude of 182°.5W with a temperature of 183.0 ± 1.3 K, whereas on March 19, the peak temperature (183.4 ± 1.3 K) instead occurs at 187°.5W. This apparent 5° longitude shift is comparable with the diffraction-limited spatial resolution at this latitude (~5° in longitude), so we cannot determine whether this apparent westward shift is physical or a result of uncertainty introduced by the spatial registration.

However, we believe the eastern region of heating centered at ~162°.5W is physical and colocated with the MAE within the uncertainty. Figure 10 shows observed and synthetic spectra and the corresponding vertical profiles of temperature at 67°.5N, 162°.5W, where the largest change in temperature between March 17 and 19 occurred. Over the range of vertical sensitivity of the observations (100 mbar $< p <$ 1 μbar), the strongest duskside heating occurs over the 40–1 μbar pressure range. For example, at 162°.5W, the temperature at 9.0 μbar increases from 170.0 ± 1.5 to 179.1 ± 1.4 K, or a difference of 9.1 ± 2.1 K. We discuss the possible mechanisms by which the arrival of the solar wind compression between March 17 and 19 (Figure 1) drove the observed heating in Section 6.

Marginal temperature increases are also observed at ~1 mbar at ~160°W when comparing results on March 17 and 19. For

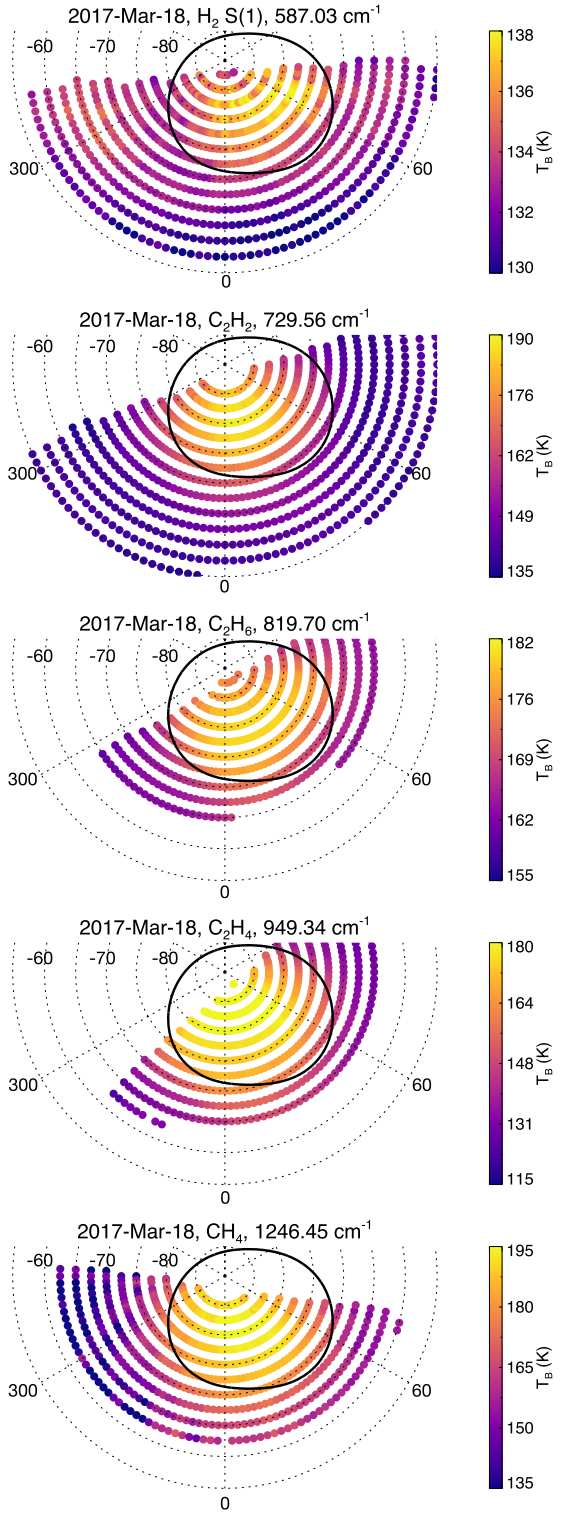

Figure 2. Distribution of coadded TEXES observations of the H_2 S(1) quadrupole (first panel), C_2H_2 (second panel), C_2H_6 (third panel), C_2H_4 (fourth panel), and CH_4 (fifth panel) emission on 2017 March 18. Points are colored by the brightness temperature of an emission line at the indicated wavenumber according to the color bar. The statistical-mean auroral oval position is shown as a solid black line (Bonfond et al. 2017).

example, at 157.°5W, we find a 1 mbar temperature difference of 3.3 ± 1.6 K or $\sim 2.1\sigma$. Given that only two locations in the 145–170°W range are just barely over the 2σ level, we consider the apparent lower stratospheric heating to be a tentative result.

5. Hydrocarbon Retrievals

The retrieved temperature distributions presented in Section 4 were adopted as the temperature profile, and the 730, 950, and 819 cm^{-1} spectra were inverted in order to retrieve the vertical profiles of C_2H_2, C_2H_4, and C_2H_6, respectively. The vertical profiles of C_2H_2, C_2H_4, and C_2H_6 shown in Figure 4 were adopted as the a priori, and nominally, a fractional uncertainty of 18% was adopted at all altitudes.

5.1. C_2H_4 Retrieval Artifacts

In our first attempts at retrieving the vertical profile of C_2H_4, we noticed unphysical discontinuities in abundance at a given altitude between neighboring spatial bins. This issue seemed to arise at locations where a significant enhancement of C_2H_4 was required with respect to a priori values in order to fit the observations. The discontinuity results from the different altitudes at which the retrieval chooses to enhance the abundance. This is exemplified in Figure C1, which shows retrievals of temperature and C_2H_4 at 72.°5N, 165°W and 162.°5W using observations recorded on 2017 March 19. At 165°W, the retrieved C_2H_4 profile exhibits the largest departure from the a priori at ~2 mbar, whereas at 162.°5W, this instead occurs at ~0.3 μbar. In plotting latitude–longitude distributions of C_2H_4 abundance at a given altitude, this results in changes of several orders of magnitude in C_2H_4 between neighboring spatial bins, which cannot be physical, since the two locations are separated by less than the diffraction-limited spatial resolution.

As shown in Figure C1, the retrieved temperature profiles at both locations are very similar, so this cannot be driving the different locations of where the retrieval chooses to enhance C_2H_4. We also note that the spectral fit to the 950 cm^{-1} spectrum, particularly to the cores of the C_2H_4 lines, is significantly better at 162.°5W ($\chi^2/n \sim 1.3$), where the C_2H_4 enhancement occurs in the upper stratosphere, compared to 165°W ($\chi^2/n \sim 2.2$), which exhibits a lower stratospheric enhancement. Our interpretation is that a subset of retrievals converge on a secondary χ^2 minimum corresponding to a peak at 2 mbar and a subset converge on a better-fitting primary χ^2 minimum corresponding to the peak at 0.3 μbar. The C_2H_4 is predicted to be more sensitive to temperature in the lower stratosphere than C_2H_2 or C_2H_6 (Moses et al. 2015), so a C_2H_4 peak in the lower stratosphere is not unexpected. However, larger temporal and spatial changes in C_2H_4 in the upper stratosphere might also be expected given the shorter photochemical lifetimes at ~0.3 μbar compared to ~2 mbar (e.g., Moses et al. 2005; Hue et al. 2018).

We tested whether the observations at 72.°5N, 165°W could still be adequately fit ($\chi^2/n \sim 1$) by allowing the retrieved C_2H_4 profile to depart from the a priori only in the upper stratosphere. We performed a set of retrievals where the uncertainty on the a priori profile was reduced to 1% at pressures higher than a given cutoff level, p_0, and set to 18% at pressures lower than and including the cutoff level. This thereby forces the retrieval to fit the spectra by varying abundances at lower pressures. We tested values of p_0 of 3, 1, 0.3, 0.1, 0.03, and 0.01 mbar, which are approximately spaced evenly in logarithmic pressure. Figure C2 shows the results of these tests. In allowing C_2H_4 to vary at all altitudes or fixing the abundance at pressures higher than 3 mbar, the retrieval chooses to modify the lower stratospheric (1–2 mbar) C_2H_4

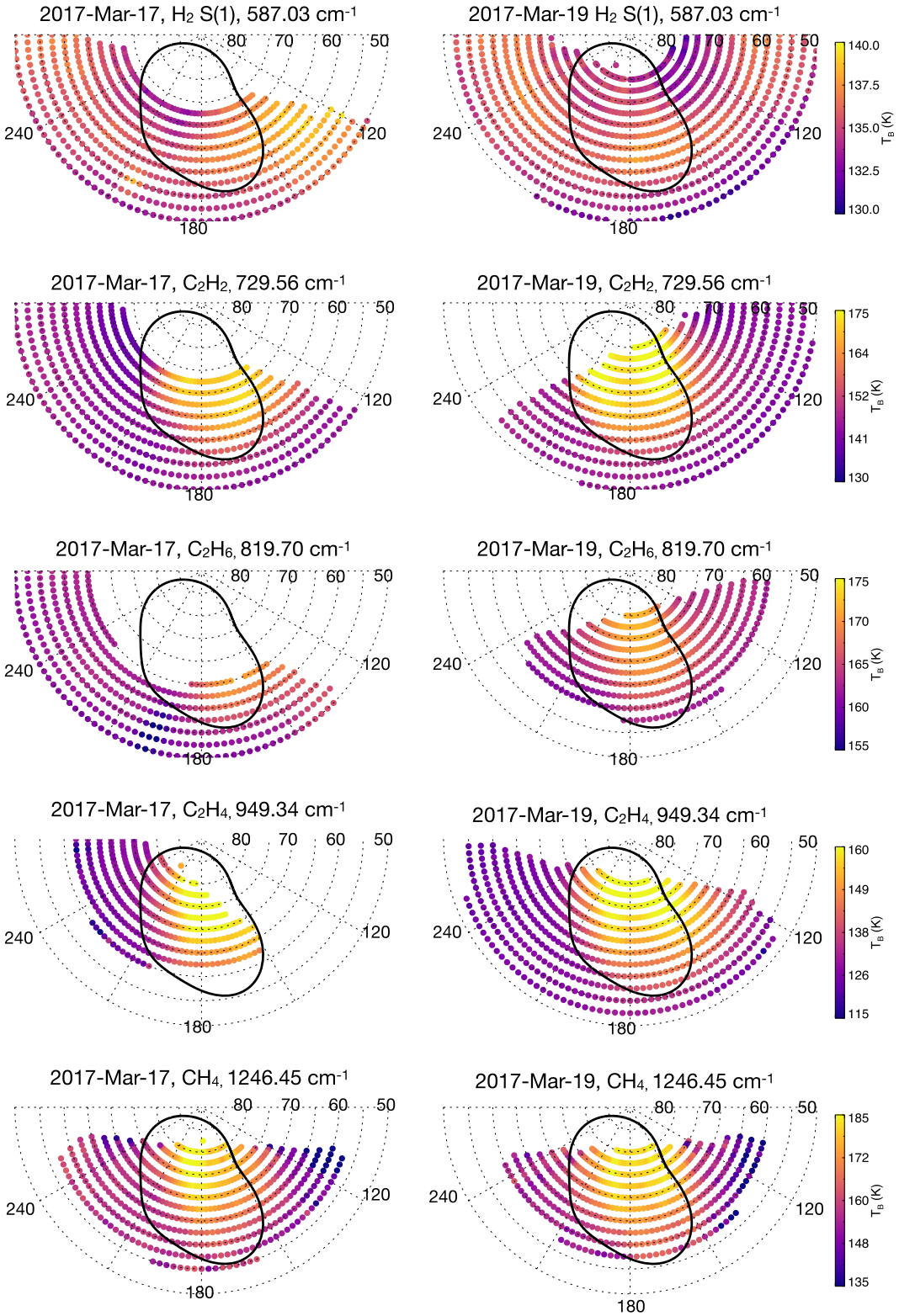

Figure 3. Distribution of coadded TEXES observations of the H_2 S(1) quadrupole (first row), C_2H_2 (second row), C_2H_6 (third row), C_2H_4 (fourth row), and CH_4 (fifth row) emission on 2017 March 17 (left column) and 19 (right column). Points are colored by the brightness temperature of an emission line at the indicated wavenumber according to the color bar. The statistical-mean auroral oval position is shown as a solid black line (Bonfond et al. 2017).

abundance with relatively little change at lower pressure levels. If the C_2H_4 abundance is fixed at pressures higher than 1, 0.3, 0.1, 0.03, or 0.01 mbar, the retrieval instead modifies the upper stratospheric C_2H_4 abundance, and the quality of the fits is significantly improved ($\chi^2/n \sim 1.1$) compared to the former ($\chi^2/n \sim 2.2$–2.5). There is negligible/zero difference in the quality of the fit to the spectra using $p_0 = 0.3$ mbar compared to $p_0 = 0.01$ mbar.

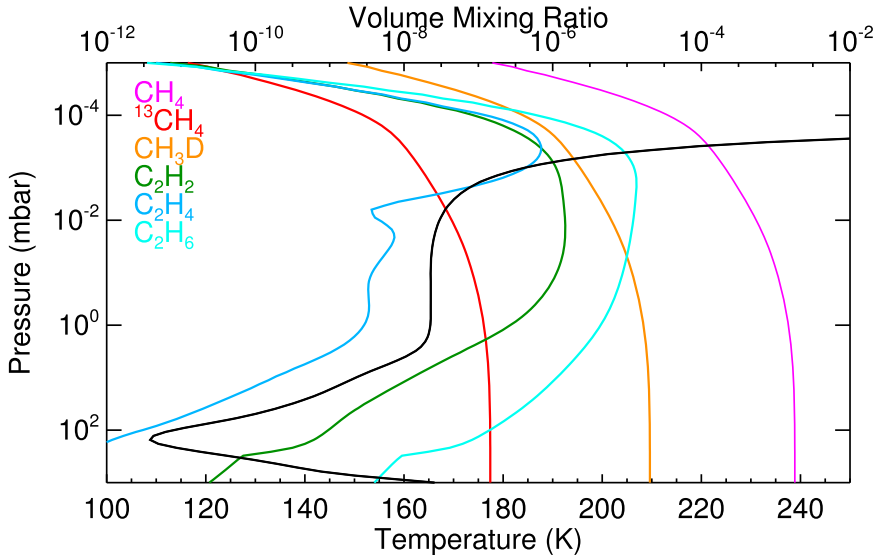

Figure 4. Vertical profile of temperature (black) according to the lower axis and vertical profiles of CH_4 (pink), $^{13}CH_4$ (red), CH_3D (orange), C_2H_2 (green), C_2H_4 (blue), and C_2H_6 (cyan) according to the upper axis. This is Model 7 from Sinclair et al. (2020), which is based on the photochemical model presented in Moses & Poppe (2017).

In summary, we find that allowing the retrieval of C_2H_4 to vary only at pressures lower than 0.3 mbar significantly improves the quality of the fit compared to adopting the nominal approach of a constant fractional uncertainty at all altitudes. This also was found to remove the discontinuities in abundances between neighboring spatial bins as noted above. We therefore adopt the a priori, where the uncertainty is set to 1% at pressures higher than 0.3 mbar, in all C_2H_4 retrievals presented in the remainder of this work.

5.2. High Southern Latitudes

Figure 11 shows the retrieved distributions of C_2H_2, C_2H_4, and C_2H_6 at high southern latitudes using observations recorded on 2017 March 18. We find that all three hydrocarbons exhibit enhancements in abundance inside the southern auroral oval, though at apparently different altitudes. This is also demonstrated in Figure 12, which compares the observed and synthetic spectra and corresponding retrieved vertical profiles at 75°S, 17.°5W and 340°W (a location inside and outside the southern auroral oval, respectively).

In general, we were able to fit the C_2H_4 emission spectra adequately well ($\chi^2/n \sim 1$) using the a priori profile detailed in Section 5.1. However, we found it challenging to adequately fit the strong emission lines of C_2H_2 and C_2H_6 in the 730 and 819 cm^{-1} settings, respectively. For example, as shown in Figure 12, the synthetic spectra struggle to fit the cores of the strong C_2H_2 emission lines at 729.56 and 729.75 cm^{-1} and the strong C_2H_6 emission line at 819.7 cm^{-1}. This was also an issue in a similar analysis of IRTF-TEXES observations recorded in 2014 December (Sinclair et al. 2018), which was attributed to non-LTE effects. We discuss both possibilities in further detail in Section 6.

For C_2H_2, the largest change in abundance between nonauroral and auroral locations occurs at ~1 mbar. At 75°S, 17.°5W (inside the southern auroral oval), we retrieve an abundance of 1.61 ± 0.13 ppmv compared to 0.04 ± 0.01 ppmv retrieved at 65°S, 340°W. For C_2H_4, the largest change in abundance between nonauroral and auroral regions occurs significantly higher in the atmosphere, at ~1 μbar, which is expected given that we modified the C_2H_4 a priori uncertainty to favor varying the upper stratospheric abundance; see Section 5.1. At 1 μbar, we retrieve an abundance of 9.68 ± 1.53 ppmv at 75°S, 17.°5W compared to 0.54 ± 0.11 ppmv at 65°S, 340°W. In contrast, C_2H_6 exhibits the largest change between nonauroral and auroral locations several decades of pressure deeper, at ~4 mbar. For example, at 4.7 mbar, the retrieved abundance of C_2H_6 exhibits an increase from 13.7 ± 1.1 ppmv at 65°S, 340°W to 25.1 ± 1.7 ppmv at 75°S, 17.°5W.

The apparent variability of C_2H_2, C_2H_4, and C_2H_6 at very different altitudes, between Jupiter's southern auroral region and a nearby nonauroral location, is puzzling. At first, we considered whether this was a retrieval artifact. However, as detailed further in Section 5.4, varying C_2H_6 abundances only in the upper stratosphere, at similar altitudes as those where C_2H_2 and C_2H_4 vary, leads to poorer fits to the spectra. We discuss this issue further in Section 6.

5.3. High Northern Latitudes

Figures 13 and 14 show the retrieved hydrocarbon distributions at high northern latitudes on March 17 and 19, respectively. On March 17, C_2H_2 exhibits two discrete regions of enriched abundances within the main auroral oval. The first region appears on the duskside of the main oval with the largest 0.01 mbar abundance of 1.31 ± 0.25 ppmv recorded at 72.°5N, 147.°5W. The second region appears slightly west of the center of the auroral region with a peak 0.01 mbar abundance of 0.93 ± 0.17 ppmv retrieved at 67.°5N, 192.°5W. In contrast to C_2H_2, the C_2H_4 on March 17 exhibits a single region of higher abundances inside the northern auroral oval and is significantly enriched compared to longitudes outside the auroral oval. For example, at 70°N, the retrieved 0.01 mbar abundances increase from 5.08 ± 0.75 ppbv at 240°W to 8.06 ± 1.18 ppbv at 175°W. Observations of C_2H_6 emission at 819 cm^{-1} on March 17 did not sample latitudes north of ~65°N. Nevertheless, for the southern part of the northern aurora that was recorded on March 17, we retrieve higher abundances toward the duskside of the main oval. For example, at 60°N, the 0.98 mbar

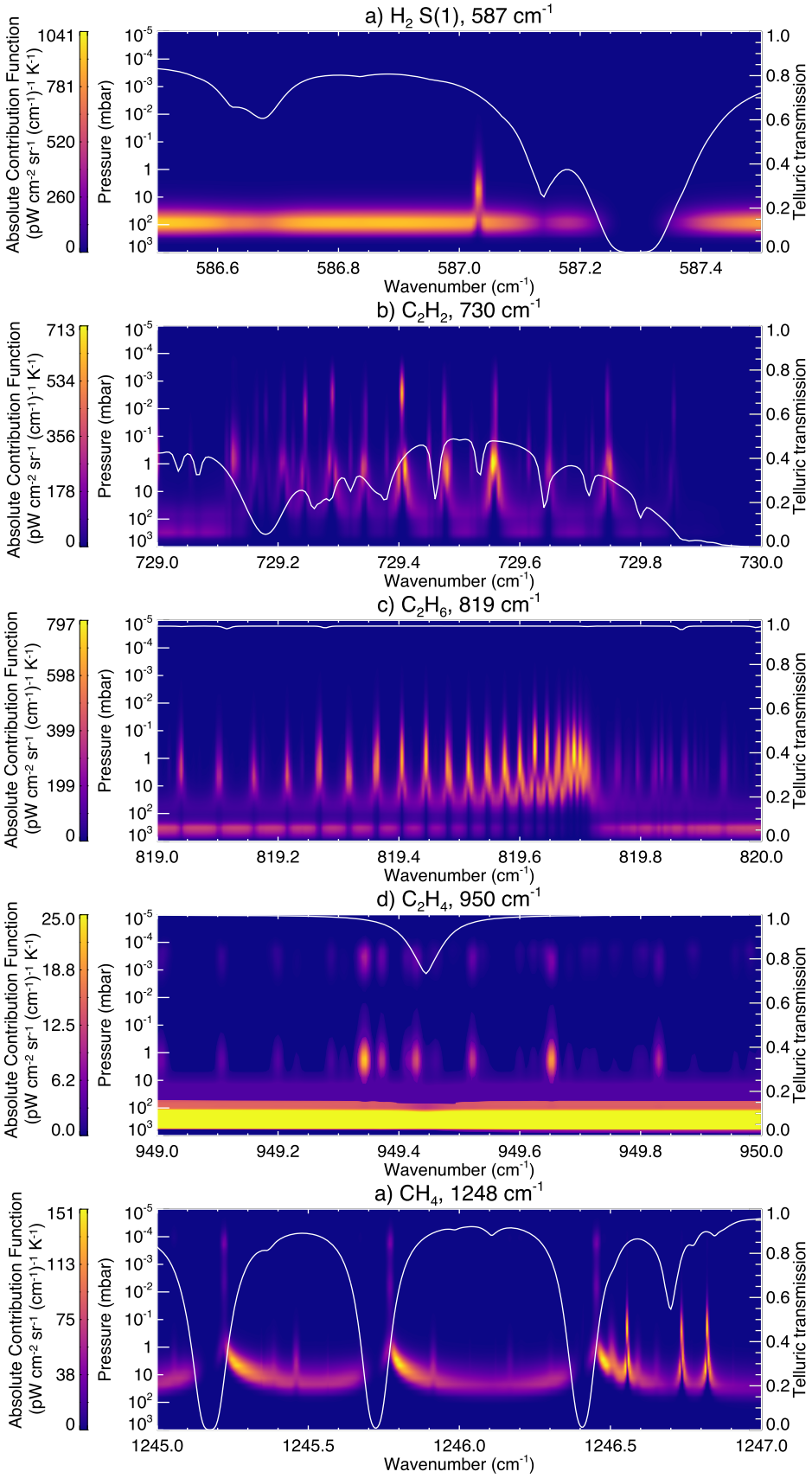

Figure 5. Vertical absolute contribution functions with respect to temperature for a subset of the (a) 587, (b) 730, (c) 819, (d) 950, and (e) 1248 cm^{-1} settings. The contribution functions have been convolved with the telluric transmission spectrum shown as a white solid line and according to the right-hand axis.

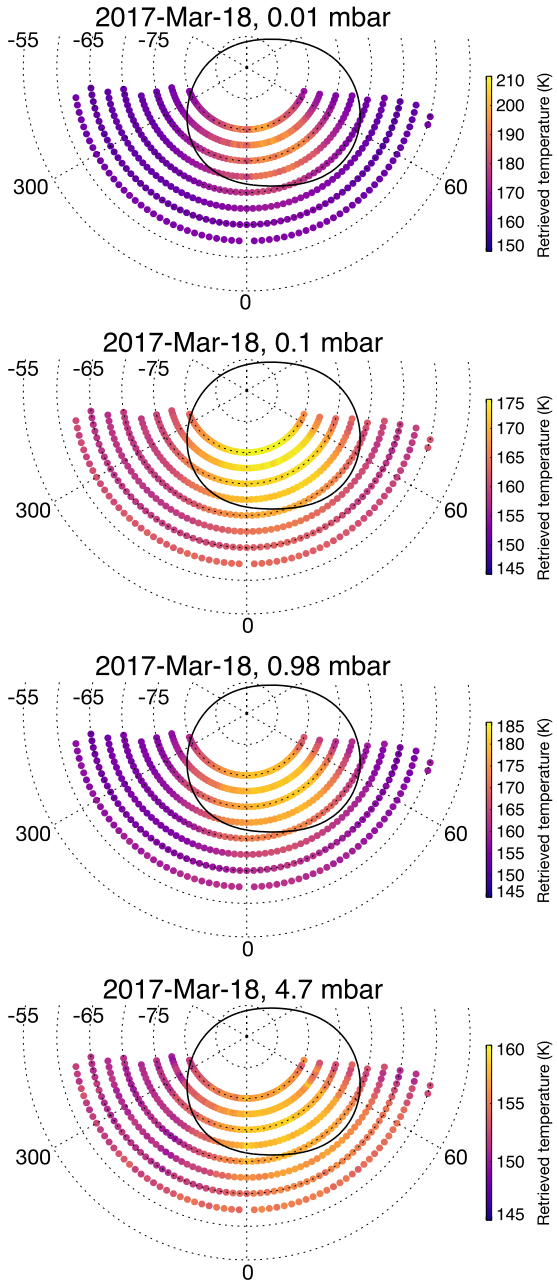

Figure 6. Retrieved temperature distributions on 2017 March 18 at 0.01 (first panel), 0.1 (second panel), 0.98 (third panel), and 4.7 mbar (fourth panel). Solid black lines denote the statistical-mean position of the ultraviolet MAE (Bonfond et al. 2017).

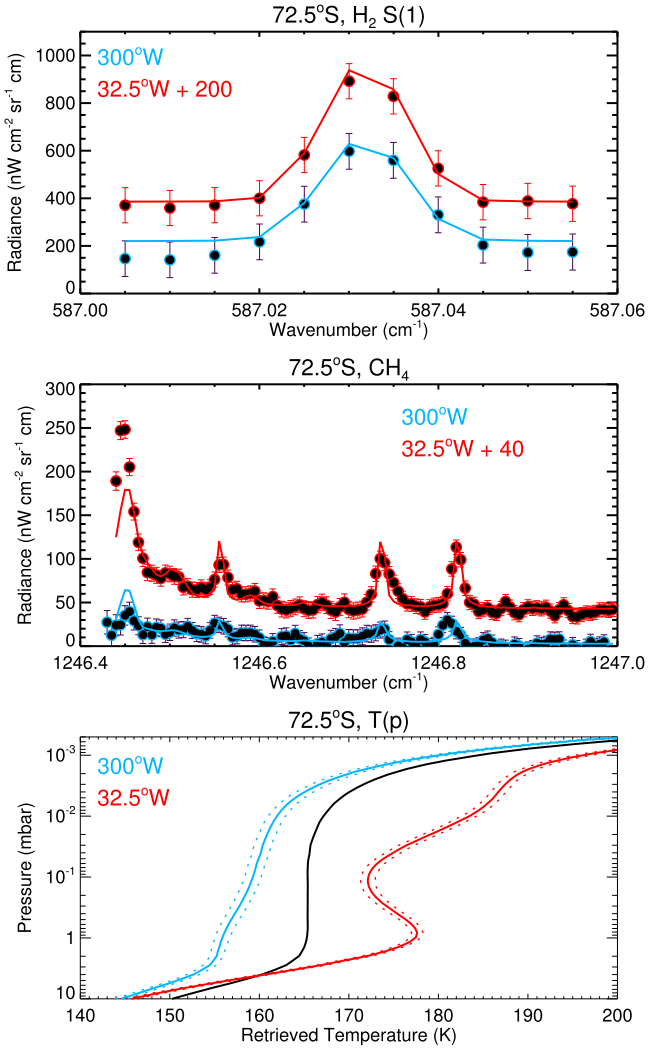

Figure 7. Comparison of observed (points with error bars) and modeled (solid lines) spectra for H_2 S(1) (top panel) and CH_4 (middle panel) emission at 72°.5S. Red and blue respectively denote results at 32°.5W (a longitude poleward of Jupiter's southern main auroral oval) and 300°W (equatorward of the MAE). An offset has been added to the red spectra for clarity. The corresponding retrieved profiles of temperature (solid lines) and uncertainty (dotted lines) are shown in the bottom panel. The black solid line denotes the initial guess or a priori profile.

abundance of C_2H_6 increases from 6.23 ± 0.97 ppmv at 240°W to 13.40 ± 1.91 ppmv at 170°W.

In comparing the retrieved distributions of C_2H_4 and C_2H_6 between March 17 and 19, we do not observe any statistically significant variability in abundance. This is also demonstrated in Figure 15, which shows longitudinal variations in C_2H_2, C_2H_4, and C_2H_6 at 72°.5N on March 17 and 19. However, we do observe significant variability in the retrieved distributions of C_2H_2 between March 17 and 19, particularly on the duskside of the main oval. For example, at 72°.5N and 162°.5W, we retrieve a 0.01 mbar abundance of 1.10 ± 0.21 ppmv on March 17 and an abundance of 3.25 ± 0.49 ppmv on March 19, which represents an increase by approximately a factor of 3. This is also spatially and vertically coincident with the ~9 K heating observed between March 17 and 19, as discussed in Section 4.2, and presumably driven by a common mechanism. As shown in Figure 16, lower stratospheric abundances of C_2H_2 at 72°.5N, 162°.5W also exhibit a smaller yet still statistically significant increase between the two dates. For example, at 0.98 mbar, the abundance increases from 397.1 ± 48.7 ppbv on March 17 to 873.6 ± 101.8 ppmv on March 19. In Section 5.4, we test whether the observations can be adequately fit by varying only upper stratospheric C_2H_2 abundances. However, we find that the best fits to the observations are achieved when 1 and 0.01 mbar abundances are both allowed to vary.

At 200°W in the same latitude band, we also observe a smaller but still significant increase in the 0.01 mbar C_2H_2 abundance from 0.91 ± 0.18 ppmv on March 17 to 1.61 ± 0.29 ppmv on March 19. This is also spatially coincident with an apparent region of heating observed between March 17 and 19, although, as discussed in Section 4, we are uncertain whether

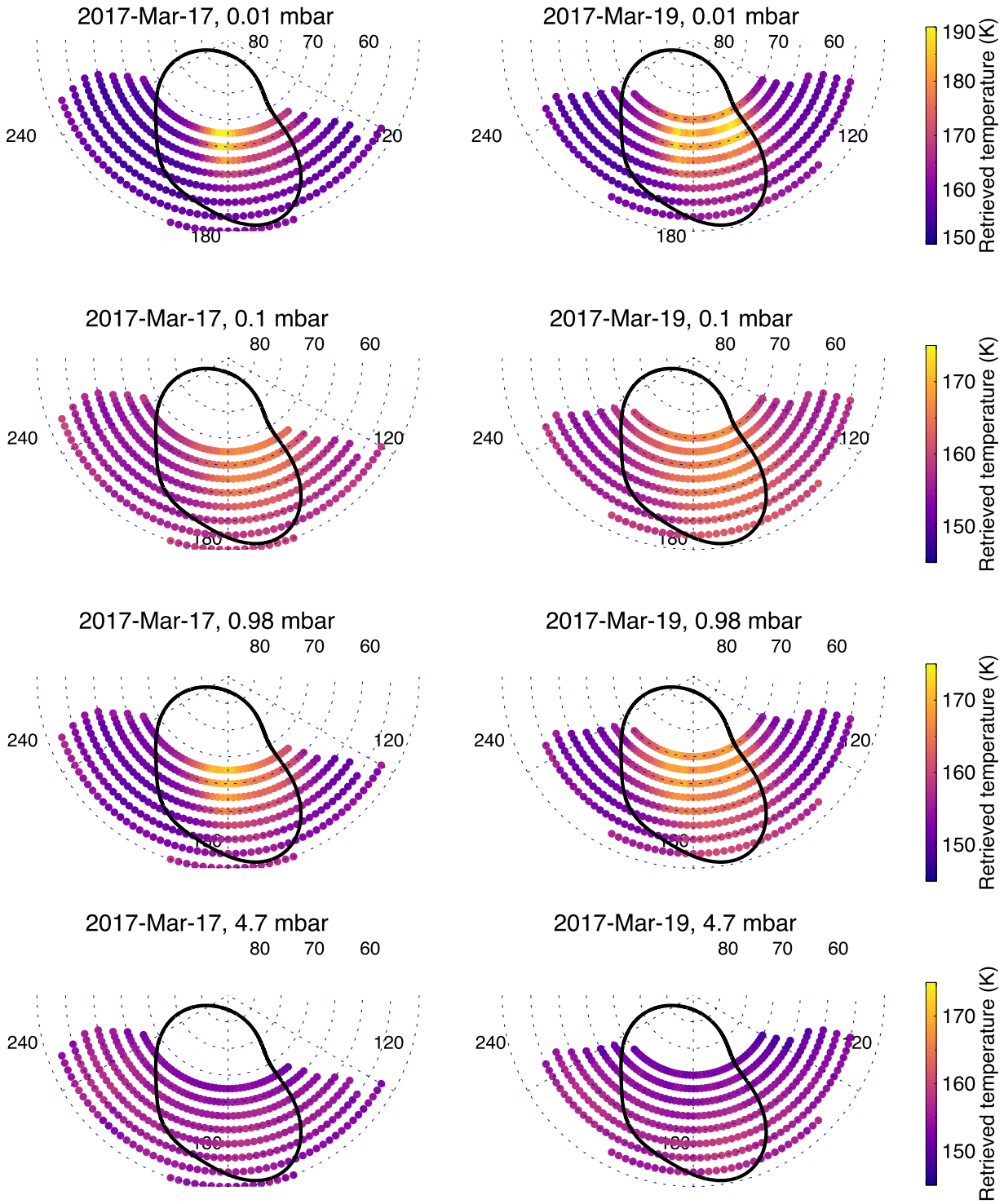

Figure 8. Retrieved temperature distributions on 2017 March 17 (left column) and 19 (right column) at 0.01 (first row), 0.1 (second row), 0.98 (third row), and 4.7 mbar (fourth row). Solid black lines denote the statistical-mean position of the ultraviolet oval (Bonfond et al. 2017).

this specific region of heating is real or an artifact of uncertainties on spatial registration. We therefore consider this region of an apparent C_2H_2 abundance increase at 200°W a tentative result.

5.4. A Priori Testing

We performed additional retrievals of C_2H_6 at 72°.5S, 17°.5W (a location inside the southern auroral oval) and C_2H_2 at 72°.5N, 162°.5W (the duskside of the northern oval) to explore the robustness of the results presented in Sections 5.2 and 5.3. While retrievals of C_2H_2, C_2H_4, and C_2H_6 show that the southern auroral oval is enriched in all three hydrocarbons compared to a location outside the oval, the enrichment of C_2H_6 is strongest in the lower stratosphere (∼4 mbar) compared to that of C_2H_2 and C_2H_4, which is stronger in the upper stratosphere (1–10 μbar). Our goal was to test whether

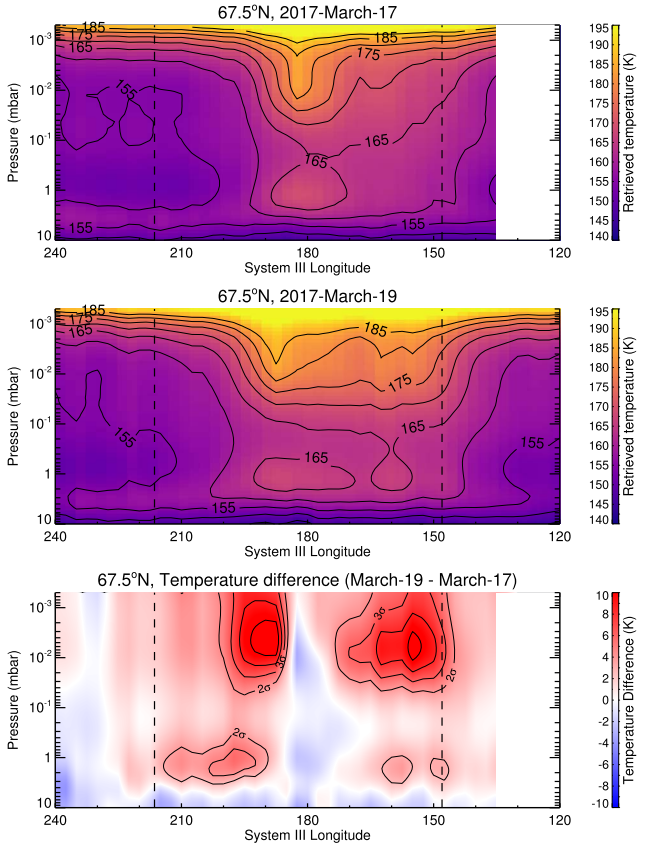

Figure 9. Longitude–pressure cross section of retrieved temperatures at 67.°5N. Results for 2017 March 17 are shown in the top panel and for March 19 in the middle panel. The temperature difference (March 19–March 17) is shown according to the color bar, and line contours mark the 2σ, 3σ, 4σ, 5σ, and 6σ levels to demonstrate where temperature changes are significant with respect to uncertainty. Vertical dashed lines correspond to the longitudinal boundaries of the auroral oval at 67.°5N.

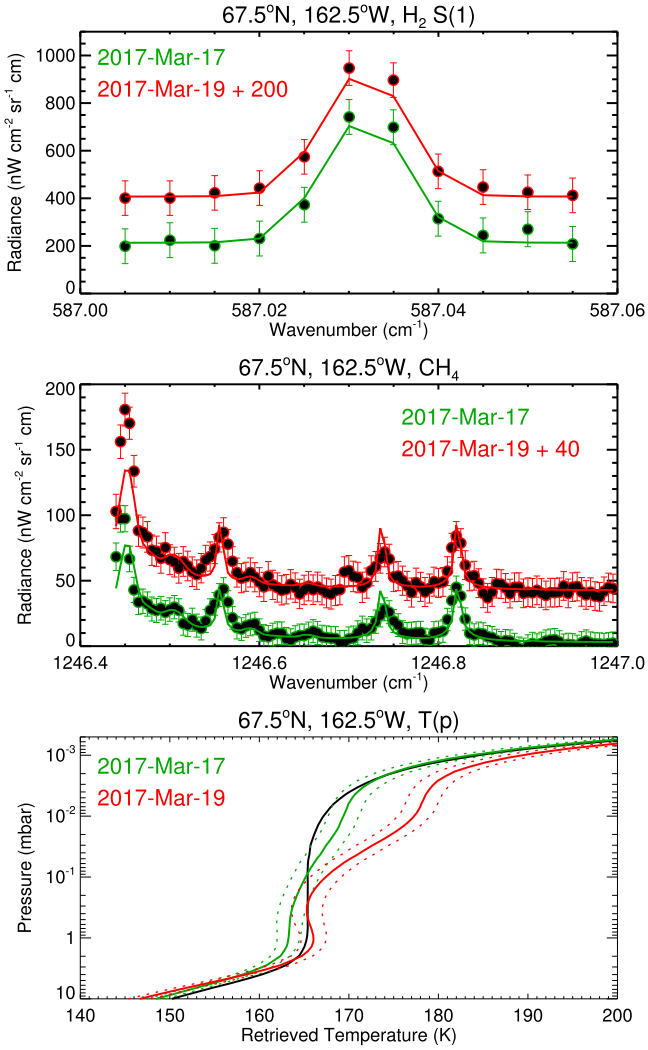

Figure 10. Comparisons of observations (points with error bars) and synthetic spectra at 67.°5N, 155°W in the 587 (top panel) and 1248 (middle panel) cm^{-1} spectral setting, which respectively capture H_2 S(1) and CH_4 emissions. The a priori (solid black line) and retrieved temperature profiles (solid colored lines) and uncertainty (dotted colored lines) are shown in the bottom panel. Green and red results denote March 17 and 19 results, respectively.

similar or improved fits to the observations of C_2H_6 could be achieved by allowing the enrichment of C_2H_6 to occur at the same altitudes as that of C_2H_2 and C_2H_4. In addition, a comparison of retrievals of C_2H_2 at 72.°5N, 162.°5W between March 17 and 19 shows an increase in abundance at both ∼1 and ∼0.01 mbar. Our goal was to test whether increasing the abundance only in the upper stratosphere could fit the observations adequately.

In order to perform these tests, we use the same approach adopted in Section 5.1, where the uncertainty on the a priori abundance is decreased significantly at pressures higher than a cutoff pressure, p_0. Again, we tested values of $p_0 = 3$, 1, 0.3, 0.1, 0.03, and 0.01 mbar. The results of these tests are shown in Figure 17.

For C_2H_6 in the southern auroral region, the profile retrieved using the nominal approach, where a constant fractional uncertainty is adopted for the a priori at all altitudes, is indeed the best-fitting solution ($\chi^2/n = 1.23$). In reducing the fractional uncertainty to 1% at pressures higher than 3 mbar, such that the retrieval is forced to vary C_2H_6 at lower pressures, the quality of fit to the spectra degrades significantly ($\chi^2/n \sim$ 2), and even poorer fits are obtained using even lower p_0 pressures. Thus, the contrast in C_2H_6 abundance between a nonauroral and an auroral location at predominantly ∼4 mbar does appear to be most consistent with the observations. This is in contrast to results for C_2H_2 and C_2H_4, which exhibit the largest spatial variation at significantly lower pressures (∼0.01 mbar).

For C_2H_2 on the duskside of the northern oval, similar quality of fits to the observations ($\chi^2/n = 2.04$) were obtained using an a priori with a constant fractional uncertainty at all altitudes or an a priori with a fractional uncertainty of 1% at pressures higher than 3 mbar. The fact that $\chi^2/n \sim 2$ represents our best-fitting solution again denotes the challenge in fitting both the weak and strong emission lines of C_2H_2. We attribute this to either non-LTE effects and/or temporal variability of the atmosphere between measurements in different spectral settings, as discussed further in Section 6. In fixing the retrieved profile at pressures higher than 1 mbar, 0.3 mbar, and so on, the quality of fit to the observations degrades ($\Delta\chi^2/n \sim 0.2$). The best-fitting retrieval corresponds to an absolute χ^2 value of 265.08. Retrieved profiles resulting in absolute χ^2 values of 265.08 + 1 = 266.08, 265.08 + 4 = 269.08, and 265.08 + 9 = 275.08 would signify the 1σ, 2σ, and 3σ confidence levels, respectively (Press et al. 1992). In fixing the a priori at pressures higher than 1, 0.3, 0.1, 0.03, and 0.01 mbar, the absolute χ^2 are 276.98, 285.97, 286.43, 287.34, and 289.34, which are all outside the 3σ confidence level relative to the best-

fitting retrieved profile. Thus, the increase in C_2H_2 abundance at 72°.5N, 162°.5W at both the 1 and 0.01 mbar levels does appear to best reproduce the observations.

6. Discussion

Spectra of Jupiter's H_2 S(1), CH_4, C_2H_2, C_2H_4, and C_2H_6 emission were recorded at Jupiter's mid-to-high latitudes using TEXES (Lacy et al. 2002) on Gemini-North on 2017 March 17–19. These measurements provided a rare combination of high spectral and spatial resolution observations that allowed the three-dimensional (latitude, longitude, altitude) distributions of temperature and hydrocarbon abundances and their variability to be constrained. Using OMNI measurements at Earth and the results of two different solar wind propagation models (Tao et al. 2005; Zieger & Hansen 2008) that calculated the flow out to Jupiter's orbit, a solar wind compression arrived at Jupiter on March 18, resulting in an increase in solar wind dynamic pressure of $\Delta p_{\rm dyn} = 0.25$–$0.45$ (depending on the model adopted). While the one-dimensional nature of such solar wind propagation models can introduce uncertainties on the timing and magnitude of downstream solar wind properties, these are expected to be <20 hr and <38%, respectively, given that Jupiter was within 50° of opposition (Zieger & Hansen 2008). Our analysis therefore captures how the stratospheric thermal structure and composition were modulated by the arrival of a solar wind compression and its perturbing effects on Jupiter's magnetosphere.

6.1. Upper Stratospheric Heating

At high northern latitudes, spectra of H_2 S(1) and CH_4 emission recorded on 2017 March 17 and 19 were inverted to derive temperature distributions and their net variability over ∼2 days (Figure 8). The difference between the temperature distributions on March 17 and 19 (Figure 10) reveals two regions of heating, predominantly in the upper stratosphere (1–10 μbar). The first appears at ∼68°N, ∼190°W with ∼5 K heating at the 1 mbar level and ∼9 K heating between 1 and 10 μbar and appears to result from a 5°N westward shift of the longitude–temperature distribution between 2017 March 17 and 19. Given that 5° in longitude is similar to the diffraction-limited spatial resolution achieved at this latitude, we consider this first region of heating to likely be an artifact of uncertainties on the spatial registration of the spectral cubes. However, we observe a second region of transient heating on the duskside of the northern oval, which we believe to be physical. The heating occurs predominantly in the upper stratosphere with a temperature increase at 9 μbar of 9.1–2.1 K at 67°.5N, 162°.5W as an example location/altitude. This location is spatially coincident with the MAE (within the uncertainty).

In Sinclair et al. (2019b), broadband 7.8 μm images of Jupiter's CH_4 emission on 2017 January 12 also captured a bright, elongated feature colocated with the northern duskside MAE. This feature was absent from images recorded less than 24 hr later, which demonstrated its transience. However, without images recorded before January 12, it could not be determined how long the feature had been present. From the same data set, Jupiter's southern auroral oval exhibited a brightening and then dimming of CH_4 emission between 2017 January 11 and 14 and contemporaneous with the northern duskside feature, which suggested that both phenomena were driven by a common mechanism. Both southern and northern phenomena were tentatively linked to the predicted arrival of a solar wind compression on approximately January 12, with the 48 hr timing uncertainty on the solar wind propagation model results hindering a more conclusive link. In this work, we believe our measurements have captured a similar brightening of the CH_4 emission on the duskside of the MAE between 2017 March 17 and 19. However, in contrast to Sinclair et al. (2019a), we can more confidently link this phenomenon to the arrival of a solar wind compression on March 18, since the propagation model timing uncertainty was less than 20 hr. A further advance of this work is that the high-resolution spectra recorded by TEXES allowed retrievals of vertical temperature profiles, which allow us to disentangle the altitudes at which temperature changes occurred.

Given that the duskside upper stratospheric heating observed in this work is horizontally and vertical coincident with the Lyα ultraviolet MAEs, we believe that their variability in response to solar wind compressions is driven by similar mechanisms. A leading theory for the generation of Jupiter's ultraviolet MAEs is the production of field-aligned currents driven by the breakdown of corotation in the magnetospheric plasma at 20–30 R_J (e.g., Hill 2001; Southwood & Kivelson 2001; Cowley et al. 2003). The currents of charged particles bombard and excite molecular hydrogen in Jupiter's atmosphere, which subsequently deexcites through Lyα emission at ∼0.12 μm. The same currents will also ultimately warm the upper atmosphere through processes including Joule heating, ion drag, and chemical heating (e.g., Grodent et al. 2001; Yates et al. 2014). However, the corotation breakdown theory would predict a dimming of the MAEs in response to solar wind forcing (e.g., Bonfond et al. 2020), whereas there is overwhelming evidence to the contrary (e.g., Clarke et al. 2009; Kita et al. 2016; Nichols et al. 2017; Kimura et al. 2018; O'Donoghue et al. 2021; Yao et al. 2022). Alternative mechanisms for coupling the solar wind to the MAEs have been suggested. This includes Kelvin–Helmholtz instabilities at the flanks of the magnetosphere due to the increased velocity shears during a solar wind enhancement (Delamere & Bagenal 2010). This allows solar wind plasma to enter the magnetosphere and drive magnetospheric flows, which ultimately accelerates the currents driving the MAEs and heating. In addition, Pan et al. (2021) found a positive correlation between ultralow-frequency wave activity and ultraviolet auroral power, which suggests that Alfvénic waves could also be a significant mechanism in coupling the magnetosphere and auroral emissions (Saur et al. 2018). Yao et al. (2019) presented near-simultaneous Juno, HST, and Hisaki measurements of Jupiter over the same period as the observations in this work. They also observed variability in the ultraviolet and kilometric wave emissions over the 2017 March 17–22 time period, which they attribute to cycles of magnetic loading and unloading of the magnetosphere at 60–80 R_J. They suggested that either auroral intensification or a current loop couples the loading and unloading events in the outer magnetosphere to the middle magnetosphere (20–30 R_J), which is the expected magnetospheric origin of the MAEs.

6.2. Lower Stratospheric Auroral-related Heating

Jupiter's northern auroral region is host to localized heating at ∼1 mbar (e.g., Figure 8), as demonstrated in previous studies (e.g., Kostiuk et al. 2016; Sinclair et al. 2017a, 2017b, 2020). A temperature minimum occurs at ∼0.1 mbar, which suggests that the 1 mbar heating is driven by a different mechanism compared to the upper stratospheric heating (Section 6.1). This interpretation is supported by the analyses of Ozak et al. (2013), Gustin

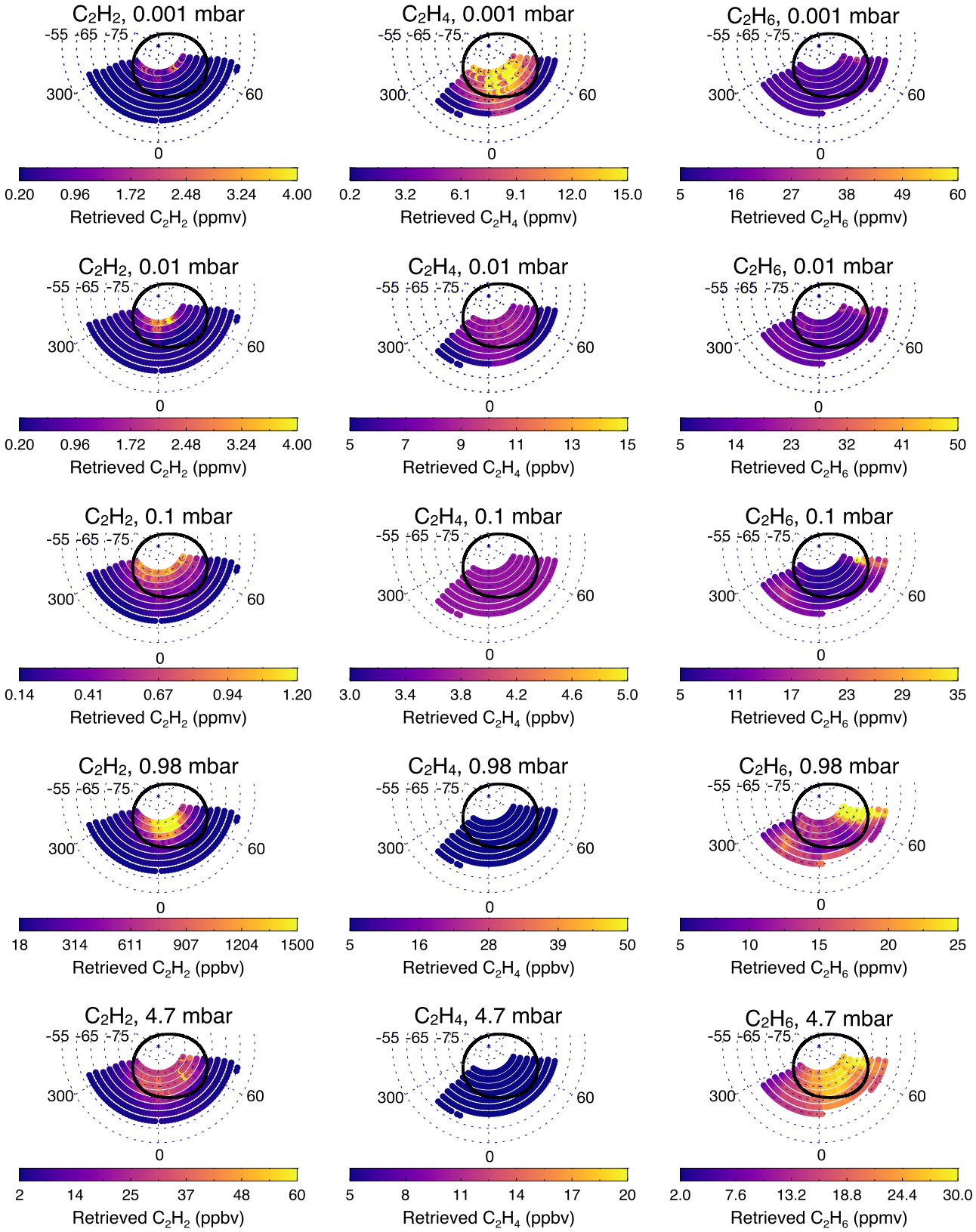

Figure 11. Retrieved abundances of C_2H_2 (left column), C_2H_4 (middle column), and C_2H_6 (right column) at high southern latitudes on 2017 March 18. Results are shown at 0.001 (first row), 0.01 (second row), 0.1 (third row), 0.98 (fourth row), and 4.7 mbar (fifth row). The solid black line denotes the statistical-mean position of the ultraviolet auroral oval (Bonfond et al. 2017).

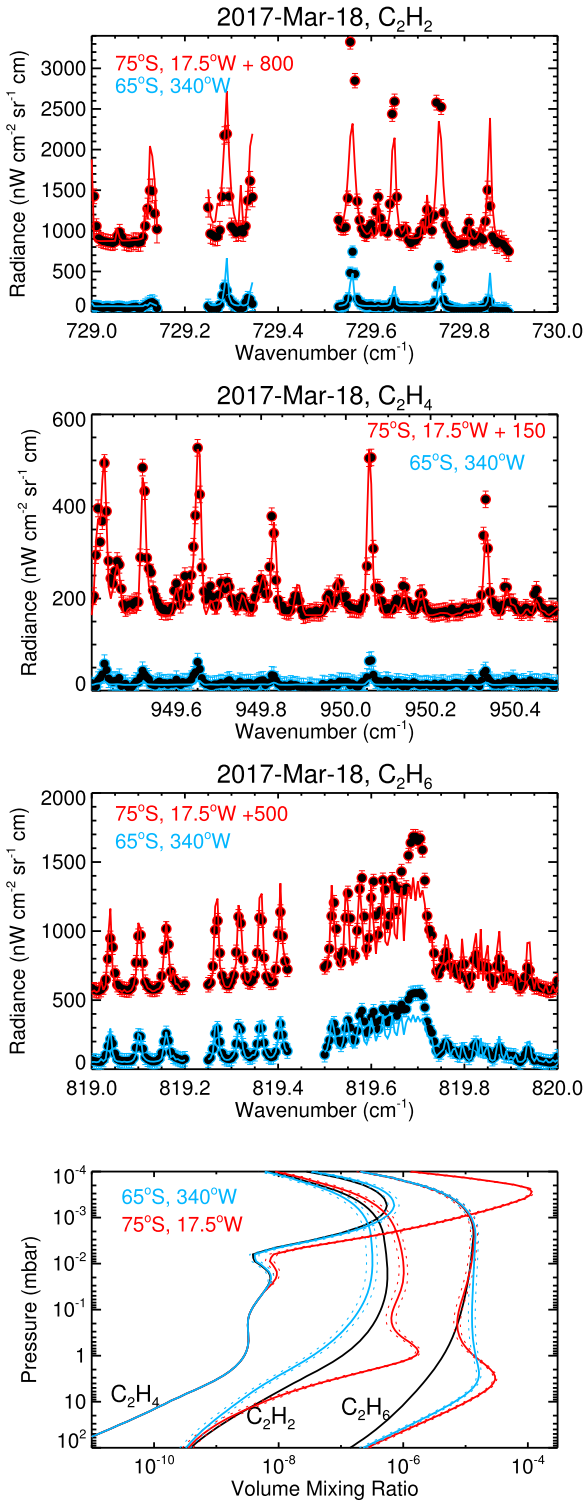

Figure 12. Comparisons of observations (points with error bars) and synthetic spectra on 2017 March 18 in the 730 (first panel), 950 (second panel), and 819 (third panel) cm^{-1} spectral settings, which respectively capture C_2H_2, C_2H_4, and C_2H_6 emissions. The a priori (solid black line) and retrieved profiles (solid colored lines) and uncertainties (dotted colored lines) are shown in the fourth panel. Blue results denote spectra/results for 65°S, 340°W, and red results denote 72.5S, 17.5W.

et al. (2016), and Houston et al. (2020), which demonstrate that energy from magnetospheric particles is not deposited deeper than 0.1 mbar or ~200 km. Indeed, at locations where significant upper stratospheric heating was observed in response to the arrival of a solar wind compression (e.g., 67.5N, 162.5W; Figure 10), there was only marginal/tentative evidence of heating deeper than 0.1 mbar in comparing March 17 and 19 results. We discuss the possible mechanisms for the 1 mbar auroral-related heating below.

The spatial resolving power provided by Gemini-North's 8 m primary, together with the relatively high southern subobserver latitude (~3.5S) at the time of the observations, has allowed for rare, high spatial and spectral resolution observations of the southern auroral oval. The southern auroral oval is otherwise challenging to sample from smaller Earth-based telescopes (with lower diffraction-limited resolutions), since it is at a relatively higher latitude compared to the northern auroral oval. In inverting spectra of the H_2 S(1) quadrupole line and CH_4 emission to retrieve the vertical temperature profile, we also find a deeper, discrete level of heating associated with the aurora. However, unlike the lower stratospheric heating in the northern auroral region, which extends to 2–3 mbar (Figure 10), lower stratospheric heating of the southern auroral region is evident at almost a decade of pressure higher, as deep as the ~10 mbar level (Figure 7). This result can also be inferred simply by comparing high southern and northern latitude maps of the H_2 S(1) quadrupole line emission (Figures B1 and B2), which sounds the 50–5 mbar level (Figure 5(a)). Heating as deep as 10 mbar was not found in previous analyses of IRTF-TEXES and Cassini-CIRS observations with limited views of the southern auroral oval (Sinclair et al. 2017a, 2018, 2020). This suggests that the presence of 10 mbar heating is a transient feature, perhaps related to the arrival of the solar wind compression at Jupiter ~6 hr earlier (Figure 1), and/or the limited spatial resolution of previous observations simply did not resolve smaller-scale regions at the high latitudes where such 10 mbar heating occurs. We favor the latter explanation, since the temperature profile at ~10 mbar is constrained predominantly by H_2 S(1) quadrupole emission at 587 cm^{-1}, which is the longest wavelength setting in this work and the most limited in spatial resolution by diffraction. Our working theory for the mechanism of the lower stratospheric heating would also rule out the former hypothesis, as detailed below.

The mechanisms responsible for the lower stratospheric auroral-related heating have proven elusive. Previous studies have suggested shortwave solar heating of haze particles (e.g., Sinclair et al. 2017a, 2018) generated by the unique chemistry inside Jupiter's auroral ovals (Wong et al. 2000; Friedson et al. 2002; Wong et al. 2003). However, we have ruled this out as the dominant mechanism responsible for the lower stratospheric auroral-related heating, since 1 mbar temperatures have been observed to vary over a larger temperature range (~20 K) and on timescales too short (<3 months) to be explained by temporal variations in solar insolation (Sinclair et al. 2018). We also considered pumping of the CH_4 3 μm band by overlapping H_3^+ emission lines from higher in the atmosphere. This would, in turn, affect the transitions responsible for the 8 μm band, a component of which originates from the ~1 mbar level. However, we have also ruled this out as a dominant mechanism because the strongest H_3^+ emissions are spatially coincident with the MAE, whereas the strongest 1 mbar heating is generally observed to be coincident with the poleward emissions.

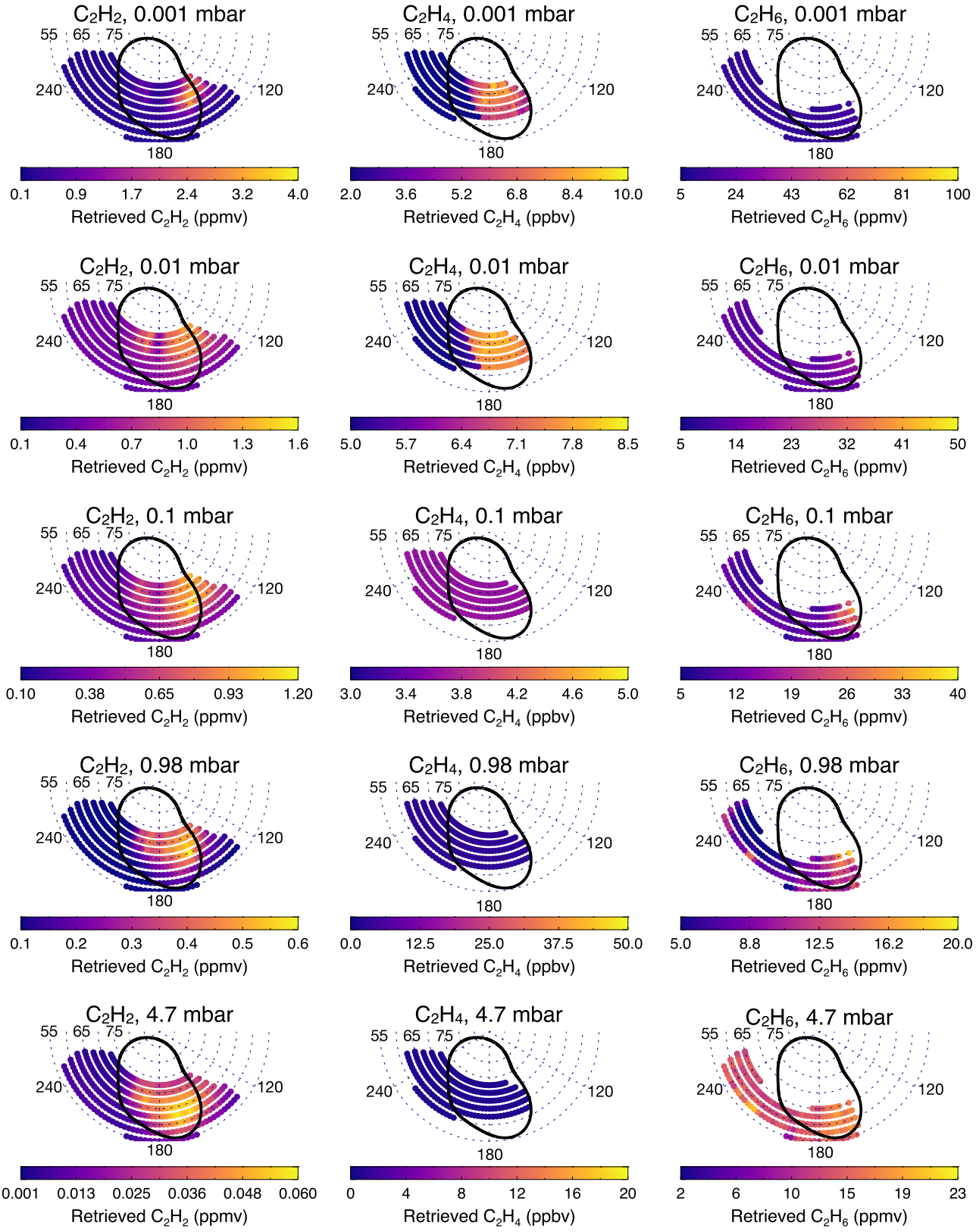

Figure 13. Retrieved abundances of C_2H_2 (left column), C_2H_4 (middle column), and C_2H_6 (right column) at high southern latitudes on 2017 March 17. Results are shown at 0.001 (first row), 0.01 (second row), 0.1 (third row), 0.98 (fourth row), and 4.7 mbar (fifth row). The solid black line denotes the statistical-mean position of the ultraviolet auroral oval (Bonfond et al. 2017).

Instead, we favor the explanation presented in a recent analysis of ALMA observations by Cavalié et al. (2021), where the Doppler shift of atmospheric lines on the limb of the planet was used to derive zonal wind velocities. Using the HCN lines, which sound ~0.1 mbar, they observed both an eastern and a western jet horizontally coincident with the southern MAE.

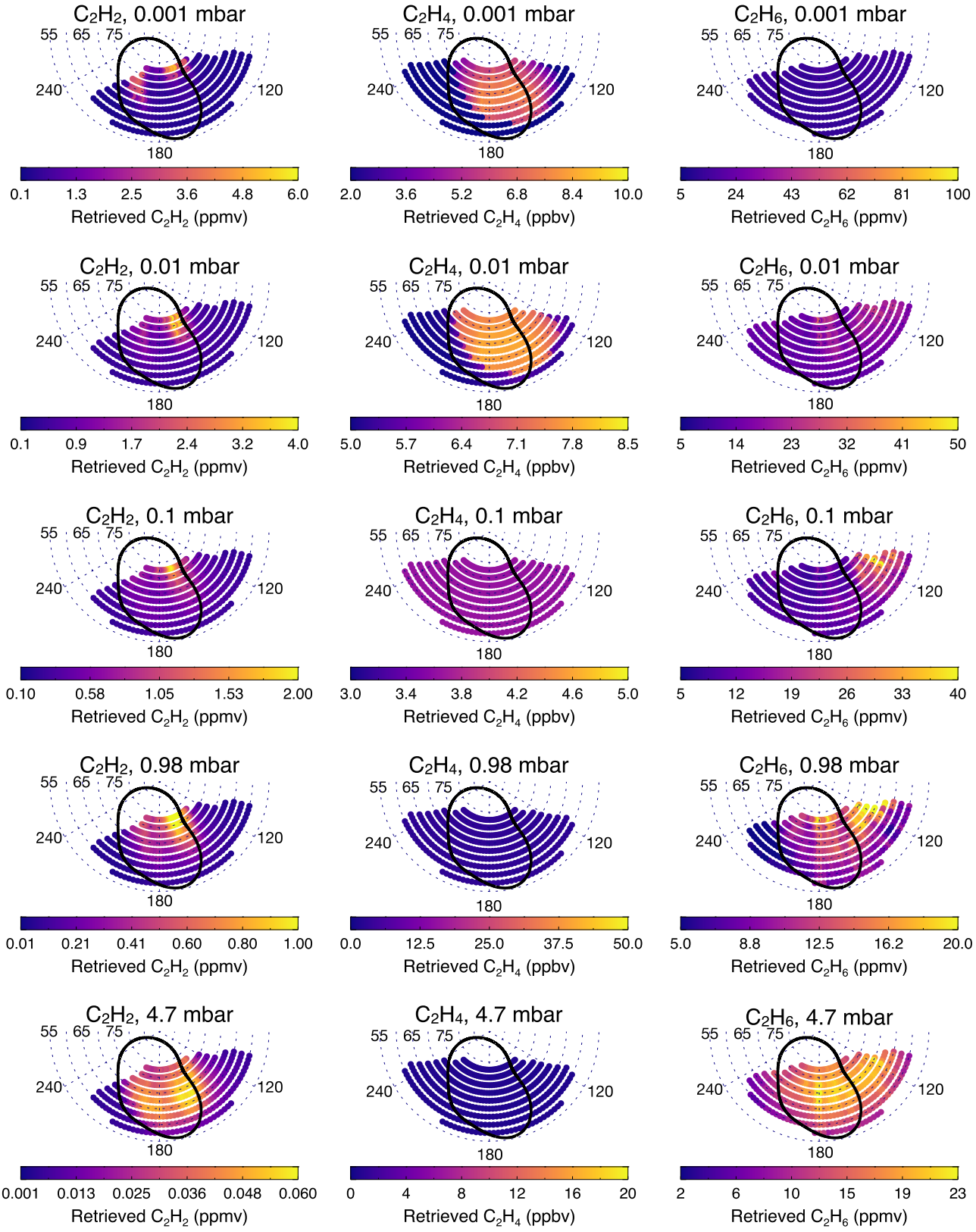

Figure 14. Same as Figure 13 but instead using observations on 2017 March 19.

These winds were inferred to have been generated from acceleration of the neutral atmosphere by energetic ions and possibly an extension of a counterrotating electrojet observed in the ionosphere (e.g., Achilleos et al. 2001; Johnson et al. 2017). Cavalié et al. (2021) interpreted that the counterrotation would result in atmospheric subsidence enclosed within the jet boundary. The compression of atmospheric gas as it descends would yield adiabatic heating deeper in the atmosphere and could be the mechanism responsible for the auroral-related lower stratospheric heating. The adiabatically heated gas would

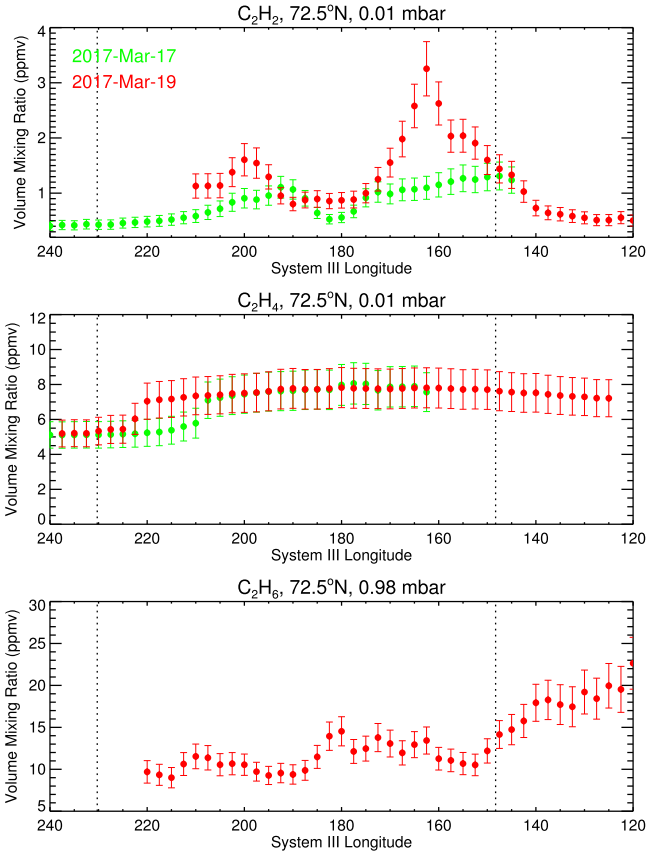

Figure 15. Longitudinal variations of retrieved C_2H_2 at 0.01 mbar (top panel), C_2H_4 at 0.01 mbar (middle panel), and C_2H_6 at 0.98 mbar (bottom panel) at 72.°5N. Results are shown at altitudes where the observations are more sensitive and thus the longitudinal/temporal variations are strongest. Results for March 17 and 19 are shown in green and red, respectively. Observations at 819 cm^{-1} on March 17 did not capture 72.°5N, so no C_2H_6 results are shown for this date. The vertical dotted lines denote the statistical-mean position of the ultraviolet main auroral oval (Bonfond et al. 2017).

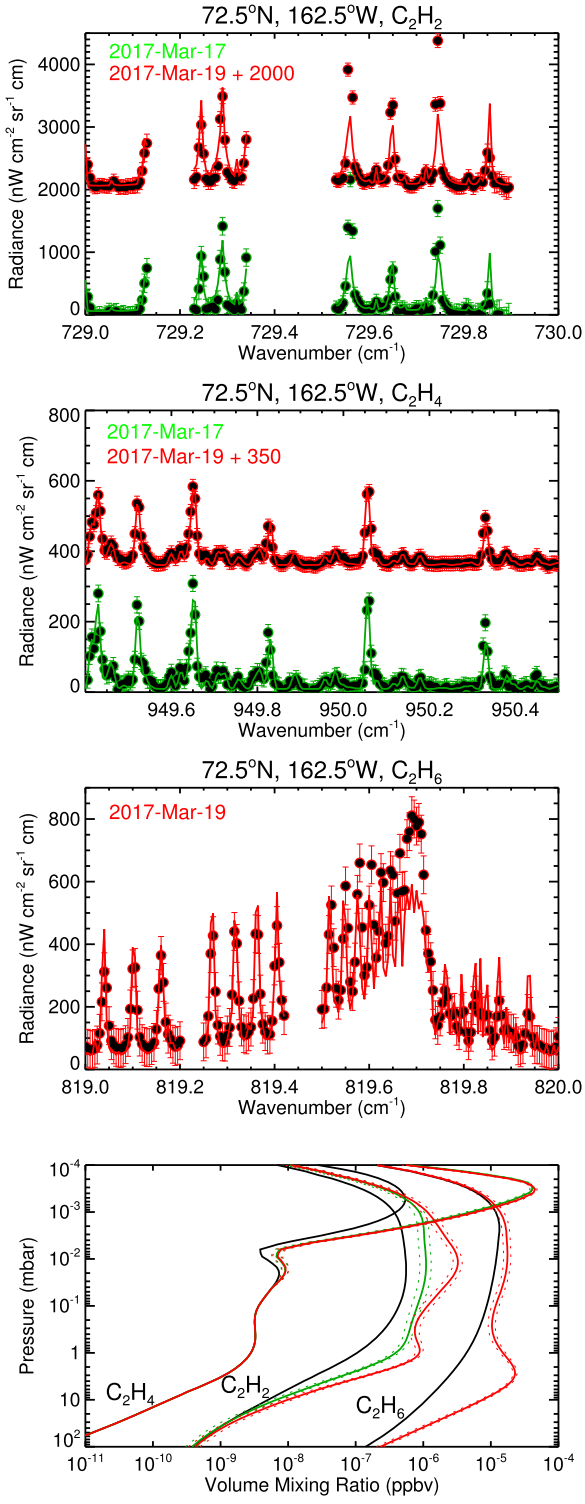

Figure 16. Comparisons of observations (points with error bars) and synthetic spectra at 72.°5N, 162.°5W in the 730 (top panel), 950 (middle panel), and 819 (bottom panel) cm^{-1} spectral settings, which respectively capture C_2H_2, C_2H_4, and C_2H_6 emissions. Only a subset of the spectral ranges inverted is shown for clarity. The a priori (solid black line) and retrieved profiles (solid colored lines) and uncertainties (dotted colored lines) are shown in the bottom panel. Green and red results denote spectra/results for March 17 and 19, respectively.

be confined inside the vortex until deeper altitudes, where the vortex would dissipate and horizontal mixing could occur. Magnetospheric flows driven by internal processes or solar wind perturbations would accelerate currents into the neutral atmosphere. This would, in turn, accelerate the vortex through ion-neutral collisions, a higher rate of subsidence, and adiabatic heating. Lower stratospheric temperatures poleward of the MAEs would therefore be expected to be modulated by magnetospheric events/solar wind conditions but with a phase lag compared to the upper stratospheric heating and ultraviolet MAEs. We believe this working hypothesis accounts for how lower stratospheric temperatures in Jupiter's auroral regions have been observed to vary on monthly timescales (Sinclair et al. 2018) but not the daily timescales demonstrated for upper stratospheric temperatures (see Section 6.1). Cavalié et al. (2021) also observed a strong westward jet at mid-northern latitudes, which may be one component of a similar counter-rotating jet coincident with the northern MAE; however, future ALMA observations would be required to conclusively determine its presence/absence.

In order to explain the stronger and deeper heating in the southern auroral oval compared to the north, we suggest the following. First, the southern auroral oval spans a smaller range in latitude/longitude; thus, energy deposited there is concentrated in a much smaller region. Additionally, the southern auroral oval overlaps with the rotational axis, so adiabatically heated gas at ∼1 mbar would be less efficiently diffused/advected horizontally, and vertical mixing would allow the warm gas to be transported deeper into the atmosphere.

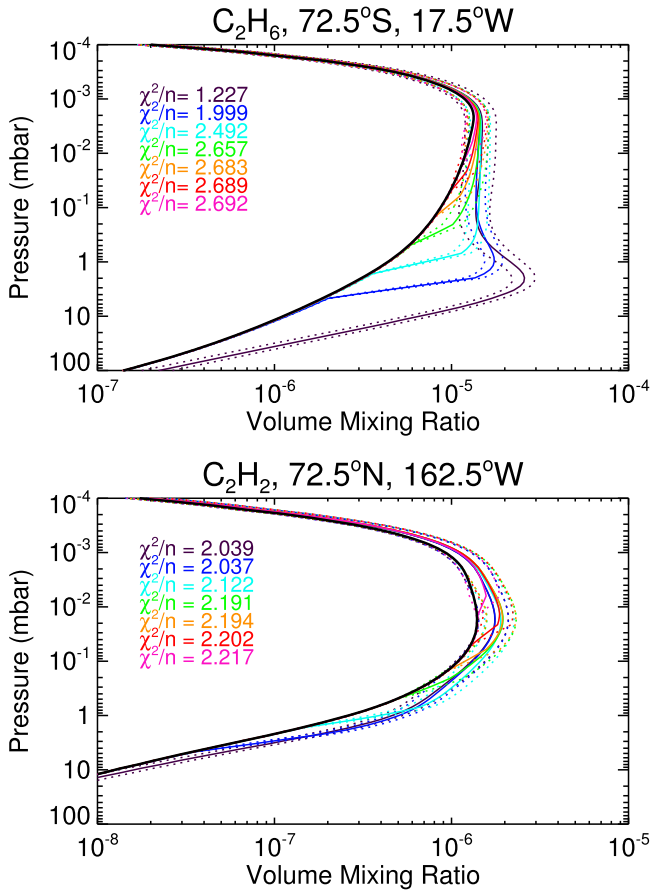

Figure 17. Test retrievals of C_2H_6 at 72.°5S, 17.°5W (top panel) and C_2H_2 at 72.°5N, 162.°5W (bottom panel). Black denotes the a priori, retrieved profiles are solid colored lines, and uncertainties on the retrieved profiles are dotted colored lines. Purple denotes the profile retrieved when an 18% fractional uncertainty is adopted at all altitudes. The remaining profiles are those retrieved when the a priori uncertainty was decreased to 1% at pressures higher than 3 (blue), 1 (cyan), 0.3 (green), 0.1 (orange), 0.03 (red), and 0.01 mbar (pink). The corresponding reduced χ^2 values are also shown in each plot.

Second, Kotsiaros et al. (2019) demonstrated that Pedersen conductivities are higher in the southern auroral oval compared to the north. Higher conductivities would allow stronger currents, greater acceleration of the neutrals and spin-up of the vortex, and, ultimately, stronger lower stratospheric heating. ALMA observations of the stratospheric winds in both auroral regions simultaneously would help to check whether or not southern auroral winds are stronger than northern ones.

6.3. Hydrocarbon Results

The magnitude of the spectral emission features of C_2H_2, C_2H_4, and C_2H_6 depend on both the vertical temperature profile and the vertical profile of the emitting molecule. Retrievals of their abundance were required in order to disentangle whether spatial/temporal variations in emission were the result of temperature changes alone or changes in both temperature and abundance. Adopting the temperature distributions inverted from the H_2 S(1) and CH_4 emission spectra, three-dimensional (longitude, latitude, altitude) distributions of C_2H_2, C_2H_4, and C_2H_6 abundances on March 17, 18, and 19 were retrieved. As detailed further in Section 5.1, we modified the a priori profile of C_2H_4 such that solutions varying only the upper stratospheric abundance would be favored in order to avoid unphysical spatial discontinuities.

In comparing retrieved hydrocarbon abundances between March 17 and 19, we found a statistically significant increase in the abundance of C_2H_2 in both the lower and upper stratosphere spatially coincident with the duskside MAE. For example, at 72.°5N, 162.°5W, we retrieve a 0.01 mbar C_2H_2 abundance of 1.10 ± 0.21 ppmv on March 17 and 3.25 ± 0.49 ppmv on March 19, approximately a threefold increase (Figures 13, 14 and 16). At the same locations and dates, the 1 mbar C_2H_2 abundance increased from 397.1 ± 48.7 to 873.6 ± 101.8 ppbv, which is a smaller fractional increase compared to that at 0.01 mbar but still statistically significant. At the intermediate level of 0.1 mbar, there was negligible change in the C_2H_2 abundance with respect to the uncertainty. As demonstrated in Section 5.4, we could not achieve the same quality of fits to the C_2H_2 emission spectra in varying only the upper stratospheric abundances; a bifurcated change in both the lower and upper stratosphere does optimize the fit to the observations (Figure 17). At this same location (72.°5N, 162.°5W), we found no statistically significant change in the C_2H_4 abundance between March 17 and 19 (Figure 16), so the duskside brightening of C_2H_4 emission appears to result from heating of the atmosphere alone. Observations of C_2H_6 emission at 819 cm^{-1} at this location were only recorded on March 19, so we cannot determine the variability of the C_2H_6 abundance between the two dates.

Observations on March 18 of the high southern latitudes provided a snapshot of the hydrocarbon abundances inside and outside the southern MAE. We found that C_2H_2, C_2H_4, and C_2H_6 all exhibit enrichments in abundance inside the southern auroral oval in comparison to a location equatorward of the southern auroral region (Figure 12). However, the altitude at which the enrichment occurs differs for each hydrocarbon.

It is very challenging to reconcile these results for several reasons. First, photochemical models of Jupiter demonstrate that the production timescale for C_2H_2 is on the order of ~100 days at 1–10 μbar, increasing to ~300 days at 1 mbar (Moses et al. 2005; Nixon et al. 2007; Hue et al. 2018). It is possible that the production timescales in the upper stratosphere may be shorter in Jupiter's auroral regions, since these models do not account for the higher rates of ion-neutral and electron-recombination reactions expected in this region (Sinclair et al. 2017a, 2019b). Nevertheless, the apparent threefold increase in C_2H_2 abundance at 0.01 mbar and twofold increase at ~1 mbar over a 2 day timescale seems unphysically large. While the vortex we suggest as the mechanism for the lower stratospheric heating (Section 6.2) would also advect hydrocarbon-richer gas to lower altitudes, we would expect such a process to be phase lagged and occur over longer timescales than ~2 days. Second, C_2H_2, C_2H_4, and C_2H_6 are strongly coupled photochemically, so it is challenging to explain the apparent increase in C_2H_2 without a corresponding increase in C_2H_4 and C_2H_6.

We suggest the following reasons to explain the physically counterintuitive hydrocarbon results described above. First, the altitude ranges of sensitivity in the 587 and 1248 cm^{-1} spectral settings used to constrain temperature and those in 730, 819, and 950 cm^{-1} used to constrain the C_2 hydrocarbon abundances differ (Figure 5). The optimal estimation technique used by the NEMESIS radiative transfer code (Irwin et al. 2008) iteratively adjusts the vertical profile of a parameter and will converge on a solution that minimizes the cost function

(Equation (1)). Thus, retrievals will favor solutions where a variable parameter is increased/decreased at altitudes of the greatest sensitivity. This, together with the degeneracy in temperature and abundance in reproducing the observed emission features, could be driving unphysical hydrocarbon solutions. Second, we expect the uncertainty on the spatial registration of the spectral cubes to be similar to the diffraction-limited spatial resolution, which corresponds to an $\sim 5^{\circ}$ latitude–longitude footprint at 60°N. Spatial offsets between the different spectral settings could mean that the emission features used to constrain temperature capture a slightly different horizontal location compared to those used to constrain hydrocarbon abundances. Third, retrievals of temperature have assumed that the vertical profile of CH_4 is horizontally homogenous. Sinclair et al. (2020) found no statistically significant variation in the vertical profile of CH_4 inside the northern auroral oval; however, it is possible that spatial variations do exist over a range smaller than the uncertainty. Our analysis would instead interpret these variations as temperature and not CH_4 abundance, which would, in turn, affect the hydrocarbon retrievals. Fourth, the downwelling suggested by the presence of a vortex (see Section 6.2) would also modify the vertical profiles of CH_4 and its photochemical by-products (Moses et al. 2015). This may also be compounded in Jupiter's auroral regions by higher rates of ion-neutral and electron-recombination reactions. The vertical shape of the hydrocarbon profiles in Jupiter's auroral regions may, therefore, be very different in reality from the photochemically predicted profiles adopted as a priori for our retrievals.

In addition, we note to readers that our radiative transfer software adopts the assumption of LTE. This describes the case where the population of the upper energy states of the rotational and vibrational modes are in equilibrium with the translational/kinetic population and therefore set by the Boltzmann distribution (and dependent on the thermodynamic temperature). Non-LTE is expected to become important at pressures lower than 0.1 mbar (Appleby 1990) due to the lower rate of intermolecular collisions. Spontaneous emission, solar pumping of lines, excitation by particle collisions, and further processes (see discussion in López-Puertas & Taylor 2001) modify the population of upper energy vibrational/rotational states away from a Boltzmann distribution; therefore, they are no longer in equilibrium with the kinetic/translational population. The paucity of intermolecular collisions at lower pressures (<0.1 mbar) means that there are insufficient energy exchanges between molecules to redistribute energy gains or losses associated with the above processes. Non-LTE effects are expected to be most noticeable for stronger lines because these correspond to a larger energy transition, which requires a greater number of intermolecular collisions to redistribute the energy lost or gained by spontaneous emission, solar pumping, and so on. We believe that this is one possible explanation of the inability to adequately fit the weak and strong emission lines of CH_4, C_2H_2, and C_2H_6 (for example, Figure 16). The assumption of LTE may also be contributing to the physically counterintuitive hydrocarbon results described above. Parameterizing non-LTE effects in the NEMESIS forward model will be the subject of future work.

7. Conclusions

We present Gemini-North/TEXES (Lacy et al. 2002) spectroscopy of Jupiter's mid-infrared H_2 S(1) quadrupole, CH_4, C_2H_2, C_2H_4, and C_2H_6 emission features at mid-to-high latitudes on 2017 March 17–19. These observations provided a rare combination of high spectral resolving power ($65{,}000 < R < 85{,}000$) and the high diffraction-limited spatial resolution provided by Gemini-North's 8 m aperture. The data capture Jupiter's mid-infrared auroral emissions before, during, and after the arrival of a solar wind compression on March 18, which allows the modulation of stratospheric temperature and composition by the external space environment to be determined. In comparing observations on March 17 and 19, we observe a brightening of the mid-infrared CH_4, C_2H_2, and C_2H_4 emissions in a region that is spatially coincident with the duskside of the northern MAE. In inverting the spectra on both nights to derive atmospheric information and variability, we find that the duskside brightening of the aforementioned emission features results (in part) from upper stratospheric ($p < 0.1$ mbar/$z > 200$ km) heating (e.g., $\Delta T = 9.1 \pm 2.1$ K at 9 μbar at 67°.5N, 162°.5W) with negligible transient heating at pressures deeper than 0.1 mbar. Our interpretation is that the arrival of the solar wind enhancement on March 18 drove magnetospheric dynamics by compression of the magnetosphere and/or viscous interactions on the magnetospheric flanks. This accelerated currents and/or generated higher Poynting fluxes by Alfvénic waves, which ultimately heated the upper stratosphere through processes including Joule heating, chemical heating, and ion-neutral collisions/drag, thereby enhancing the mid-infrared emission features of the aforementioned hydrocarbons. We therefore suggest that mid-infrared observations of Jupiter's auroral regions also serve as a metric of magnetospheric dynamics at wavelengths accessible from ground-based telescopes. Using observations on March 18, retrievals of the vertical temperature profile in a region poleward of the southern MAE demonstrate auroral-related heating as deep as $\sim$10 mbar. This is almost a decade of pressure higher than similar auroral-related heating poleward of the northern MAE. We believe the deeper heating in the south results from one or a combination of (1) higher Pedersen conductivities, which generate stronger currents and acceleration of the neutrals; (2) the energy being concentrated in a smaller region; and (3) being at a relatively higher latitude and overlapping with the rotational axis, which favors the dissipation of heat through vertical mixing instead of horizontal advection/diffusion.

The research was carried out at the Jet Propulsion Laboratory, California Institute of Technology, under a contract with the National Aeronautics and Space Administration (NASA). The material is based upon work supported by NASA under grant NNH17ZDA001N issued through the Solar System Observations Planetary Astronomy program. The High Performance Computing resources used in this investigation were provided by funding from the JPL Information and Technology Solutions Directorate. The IRTF is operated by the University of Hawaii under contract NNH14CK55B with NASA. J.M. acknowledges support from NASA Solar System Workings program 80NSSC20K0462. L.N.F. was supported by a Royal Society Research Fellowship and European Research Council Consolidator Grant (under the European Union's Horizon 2020 research and innovation program, grant

agreement No. 723890) at the University of Leicester. Coinvestigator C.T. acknowledges support by MEXT/JSPS KAKENHI grant 19H01948. V.H. acknowledges support from the French government under the France 2030 investment plan as part of the Initiative d'Excellence d'Aix-Marseille Université —A*MIDEX AMX-22-CPJ-04. The analysis is based on observations obtained at the international Gemini Observatory, a program of NSF's NOIRLab, which is managed by the Association of Universities for Research in Astronomy (AURA) under a cooperative agreement with the National Science Foundation on behalf of the Gemini Observatory partnership: the National Science Foundation (United States), National Research Council (Canada), Agencia Nacional de Investigación y Desarrollo (Chile), Ministerio de Ciencia, Tecnología e Innovación (Argentina), Ministério da Ciência, Tecnologia, Inovações e Comunicações (Brazil), and Korea Astronomy and Space Science Institute (Republic of Korea). T. C. acknowledges funding from CNES and the Programme National de Planétologie (PNP) of CNRS/INSU.

Simulation results have been provided by the Community Coordinated Modeling Center at Goddard Space Flight Center through their publicly available simulation services (https://ccmc.gsfc.nasa.gov). The mSWiM model was developed by Kenneth Hansen at the University of Michigan.

Facilities: Gemini-North, TEXES (Texas Echelon Cross Echelle Spectrograph; Lacy et al. 2002).

Software: NEMESIS (Irwin et al. 2008), mSWiM (Zieger & Hansen 2008), Tao et al. (2005) solar wind model.

Data Availability Statement

The Gemini-TEXES observations presented in this work are publicly available at the Gemini Observatory Archive.[11] However, spatially mapped and absolutely calibrated versions of the observations can be requested from the authors.

Appendix A
Observation Details

Table A1 provides details of the Gemini-TEXES observations presented in this paper.

[11] https://archive.gemini.edu/searchform

Table A1
Details of the Observations Measured on 2017 March 17–19, in Chronological Order

Date	Time	File Name (jup.X.Y)	Setting (cm^{-1})	Number of Spectra	Airmass	v_{rad} ($km\ s^{-1}$)	Hemisphere	CML
	09:13:20	**7017.01**	**1248**	**890**	**1.52**	**−12.0**	**N**	**180**
	09:18:52	**7018.01**	**1248**	**890**	**1.49**	**−11.9**	**N**	**183**
	09:18:52	**7018.02**	**1248**	**625**	**1.49**	**−11.9**	**N**	**186**
	09:27:34	7019.01	1248	1371	1.44	−11.9	S	189
	09:27:34	7019.02	1248	1091	1.44	−11.9	S	192
	09:40:32	**7020.01**	**587**	**2531**	**1.37**	**−11.9**	**N**	**196**
	09:40:32	**7020.02**	**587**	**2484**	**1.37**	**−11.9**	**N**	**200**
	09:51:56	**7021.01**	**730**	**2544**	**1.33**	**−11.9**	**N**	**203**
	09:51:56	**7021.02**	**730**	**2501**	**1.33**	**−11.9**	**N**	**207**
	10:03:44	**7022.01**	**819**	**1413**	**1.28**	**−11.9**	**N**	**210**
	10:03:44	7022.02	819	1531	1.28	−11.9	N	214
	10:15:15	**7023.01**	**950**	**487**	**1.25**	**−11.8**	**N**	**217**
	10:15:15	**7023.02**	**950**	**522**	**1.25**	**−11.8**	**N**	**219**
	10:24:01	7024.01	950	1005	1.23	−11.8	S	223
2017 Mar 17	10:24:01	7024.02	950	729	1.23	−11.8	S	225
	10:33:25	7025.01	1248	850	1.20	−11.8	N	228
	10:38:41	7026.01	1248	593	1.19	−11.8	N	231
	10:38:41	7026.02	1248	626	1.19	−11.8	N	234
	10:47:21	7027.01	1248	737	1.17	−11.8	S	237
	10:47:21	7027.02	1248	773	1.17	−11.8	S	240
	10:57:41	7029.01	587	2024	1.16	−11.7	N	243
	10:57:41	7029.02	587	1054	1.16	−11.7	N	246
	11:06:38	7030.01	587	1683	1.15	−11.7	S	249
	11:06:38	7030.02	587	1683	1.15	−11.7	S	252
	11:17:32	7031.01	730	1805	1.13	−11.7	N	255
	11:17:32	7031.02	730	1903	1.13	−11.7	N	258
	11:26:59	7032.01	730	1759	1.13	−11.7	S	261
	11:26:59	7032.02	730	1759	1.13	−11.7	S	264
	11:37:00	7033.01	819	537	1.12	−11.7	N	266
	11:37:00	7033.02	819	532	1.12	−11.7	N	269
	11:46:49	7034.01	819	674	1.12	−11.6	S	271
	11:46:49	7034.02	819	678	1.12	−11.6	S	273
	11:56:21	7035.01	950	809	1.11	−11.6	N	278
	12:01:19	7036.01	950	809	1.11	−11.6	N	281
	12:06:18	7037.01	950	809	1.11	−11.6	N	284
	12:11:16	7038.01	950	846	1.11	−11.6	S	280
	12:11:16	7038.02	950	808	1.11	−11.6	S	281
	12:20:38	7039.01	1248	665	1.12	−11.6	N	291
	12:20:38	7039.02	1248	665	1.12	−11.6	N	293
	12:29:19	7040.01	1248	774	1.12	−11.5	S	284
	12:29:19	7040.02	1248	815	1.12	−11.5	S	284
	12:39:37	7041.01	587	2023	1.13	−11.5	N	298
	12:39:37	7041.02	587	1944	1.13	−11.5	N	299
2017 Mar 17	12:49:34	7042.01	587	1245	1.14	−11.5	S	288
	12:49:34	7042.02	587	1139	1.14	−11.5	S	288
	13:02:07	7043.01	730	1664	1.16	−11.5	N	304
	13:02:07	7043.02	730	1608	1.16	−11.5	N	305
	13:12:07	7044.01	730	1826	1.17	−11.4	S	291
	13:12:07	7044.02	730	1806	1.17	−11.4	S	290
	13:22:42	7045.01	819	495	1.19	−11.4	N	309
	13:22:42	7045.02	819	470	1.19	−11.4	N	310
	13:31:24	7046.01	819	715	1.21	−11.4	S	285
	13:31:24	7046.02	819	703	1.21	−11.4	S	285
	13:40:53	7047.01	950	697	1.23	−11.4	N	307
	13:40:53	7047.02	950	697	1.23	−11.4	N	307
	13:49:49	7048.01	950	849	1.26	−11.4	S	282
	13:49:49	7048.02	950	843	1.26	−11.4	S	281
	09:37:02	8005.01	1248	676	1.37	−11.4	N	307
	09:37:02	8005.02	1248	784	1.37	−11.4	N	305
2017 Mar 18	09:45:46	8006.01	1248	825	1.33	−11.4	S	279
	09:45:46	8006.02	1248	783	1.33	−11.4	S	278
	09:55:49	8007.01	587	1471	1.30	−11.4	N	295
	09:55:49	8007.02	587	1513	1.30	−11.4	N	281

Table A1
(Continued)

Date	Time	File Name (jup.X.Y)	Setting (cm^{-1})	Number of Spectra	Airmass	v_{rad} ($km\ s^{-1}$)	Hemisphere	CML
	10:05:46	**8008.01**	**587**	**1329**	**1.26**	**−11.4**	**S**	**84**
	10:05:46	**8008.02**	**587**	**1384**	**1.26**	**−11.4**	**S**	**81**
	10:20:43	8009.01	730	1625	1.22	−11.3	N	58
	10:20:43	8009.02	730	1720	1.22	−11.3	N	56
	10:30:44	**8010.01**	**730**	**1578**	**1.20**	**−11.3**	**S**	**72**
	10:30:44	**8010.02**	**730**	**1605**	**1.20**	**−11.3**	**S**	**71**
	10:41:42	8011.01	819	686	1.18	−11.3	N	52
	10:41:42	8011.02	819	735	1.18	−11.3	N	52
2017 Mar 18	**10:50:24**	**8012.01**	**819**	**625**	**1.16**	**−11.3**	**S**	**75**
	10:50:24	**8012.02**	**819**	**580**	**1.16**	**−11.3**	**S**	**75**
	10:59:46	8013.01	950	782	1.15	−11.2	N	53
	10:59:46	8013.02	950	900	1.15	−11.2	N	53
	11:08:32	**8014.01**	**950**	**674**	**1.14**	**−11.2**	**S**	**74**
	11:08:32	**8014.02**	**950**	**707**	**1.14**	**−11.2**	**S**	**73**
	11:18:09	**8015.01**	**1248**	**784**	**1.13**	**−11.2**	**S**	**74**
	11:18:09	**8015.02**	**1248**	**827**	**1.13**	**−11.2**	**S**	**73**
	11:26:55	8016.01	1248	751	1.12	−11.2	N	58
	08:58:14	9000.01	1248	730	1.56	−11.0	N	112
	08:58:14	9000.02	1248	754	1.56	−11.0	N	114
	09:06:57	9001.01	1248	882	1.50	−11.0	S	118
	09:06:57	9001.02	1248	843	1.50	−11.0	S	121
	09:16:45	9002.01	950	877	1.45	−11.0	N	123
	09:21:33	9003.01	950	837	1.42	−11.0	N	126
	09:21:33	9003.02	950	839	1.42	−11.0	N	129
	09:30:19	9004.01	950	872	1.38	−10.9	S	133
2017 Mar 19	09:30:19	9004.02	950	875	1.38	−10.9	S	135
	09:40:09	**9005.01**	**587**	**1488**	**1.34**	**−10.9**	**N**	**137**
	09:40:09	**9005.02**	**587**	**1580**	**1.34**	**−10.9**	**N**	**141**
	09:50:00	9006.01	587	1508	1.30	−10.9	S	144
	09:50:00	9006.02	587	1561	1.30	−10.9	S	147
	10:01:31	**9007.01**	**730**	**1561**	**1.26**	**−10.9**	**N**	**150**
	10:01:31	**9007.02**	**730**	**1561**	**1.26**	**−10.9**	**N**	**154**
	10:11:28	9008.01	730	1796	1.24	−10.9	S	157
	10:11:28	9008.02	730	1849	1.24	−10.9	S	160
	10:22:15	**9009.01**	**819**	**667**	**1.21**	**−10.8**	**N**	**163**
	10:22:15	**9009.02**	**819**	**702**	**1.21**	**−10.8**	**N**	**166**
	10:30:57	9010.01	819	748	1.19	−10.8	S	169
	10:30:57	9010.02	819	779	1.19	−10.8	S	172
	10:40:56	**9011.01**	**1248**	**730**	**1.17**	**−10.8**	**N**	**174**
	10:40:56	**9011.02**	**1248**	**730**	**1.17**	**−10.8**	**N**	**177**
	10:49:36	9012.01	1248	923	1.16	−10.8	S	180
	10:49:36	9012.02	1248	882	1.16	−10.8	S	183
	10:59:13	**9013.01**	**1248**	**720**	**1.14**	**−10.8**	**N**	**186**
2017 Mar 19	**10:59:13**	**9013.02**	**1248**	**801**	**1.14**	**−10.8**	**N**	**187**
	11:08:09	**9014.01**	**950**	**1326**	**1.13**	**−10.7**	**N**	**190**
	11:08:09	9014.02	950	1326	1.13	−10.7	N	193
	11:16:53	9015.01	950	956	1.13	−10.7	S	197
	11:16:53	9015.02	950	956	1.13	−10.7	S	199
	11:26:50	**9016.01**	**587**	**1464**	**1.12**	**−10.7**	**N**	**202**
	11:26:50	**9016.02**	**587**	**1417**	**1.12**	**−10.7**	**N**	**205**
	11:37:48	9017.01	730	1513	1.11	−10.7	N	208
	11:37:48	9017.02	730	1562	1.11	−10.7	N	212
	11:48:15	9018.01	819	597	1.11	−10.6	N	214

Note. All dates/times are UTC, and CML stands for central meridian longitude in System III. Observations in bold are those chosen for coaddition and analysis, as detailed in the text.

Appendix B
Individual Observations

Figures B1 and B2 respectively show northern and southern polar projection maps of radiance of the H_2 S(1) quadrupole line feature. Figures B3–B10 show similar maps for the emission features of C_2H_2, C_2H_6, C_2H_4 and CH_4.

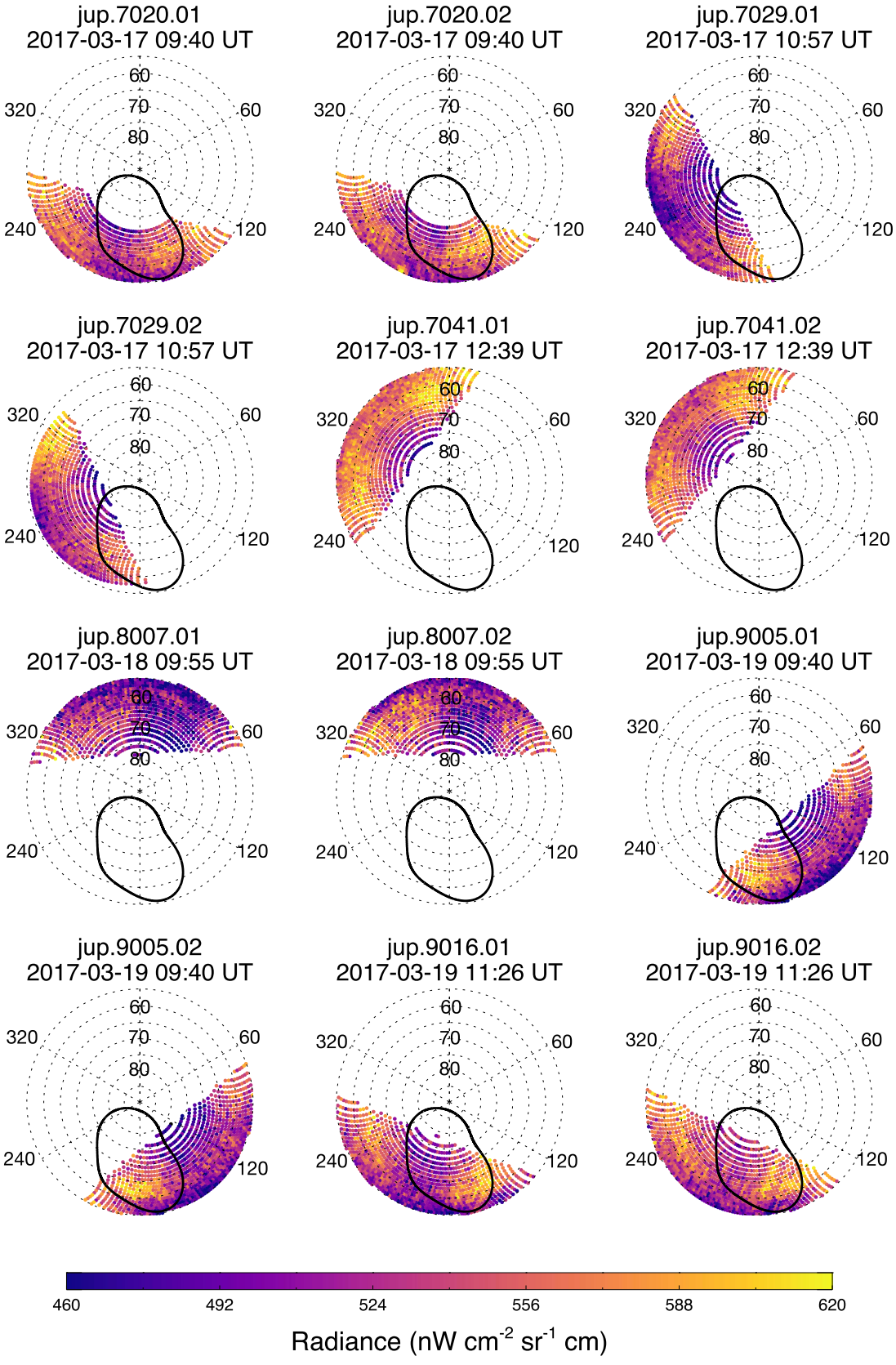

Figure B1. Individual TEXES scans of high northern latitudes. Each point represents a spectrum and is colored according to the radiance from 587.0275 to 587.0375 cm^{-1}, which captures the H_2 S(1) quadrupole emission feature. Scans are shown in chronological order from left to right and top to bottom. Solid black lines represent the statistical-mean position of the ultraviolet auroral ovals (Bonfond et al. 2017).

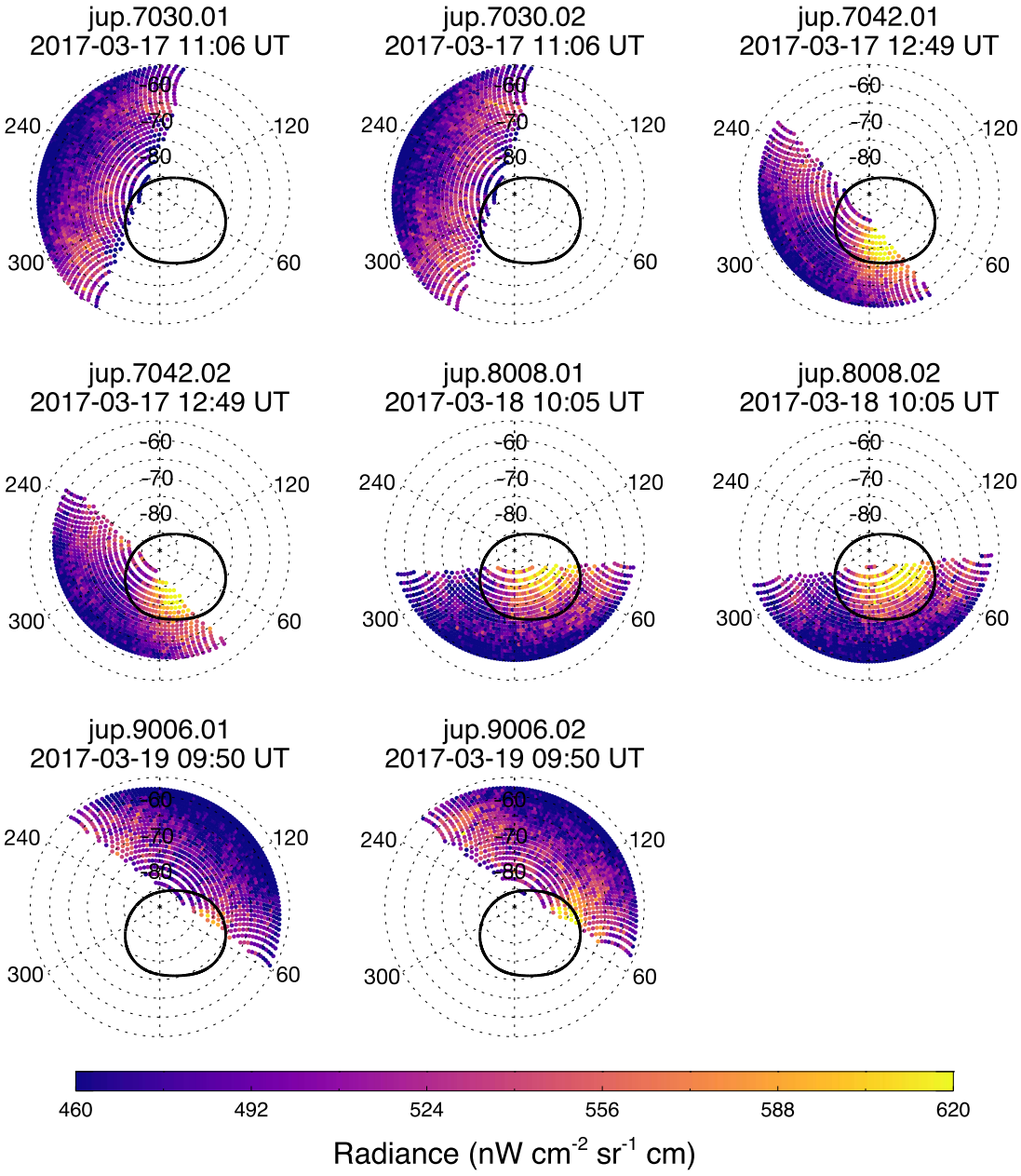

Figure B2. Same as Figure B1 but for observations of high southern latitudes.

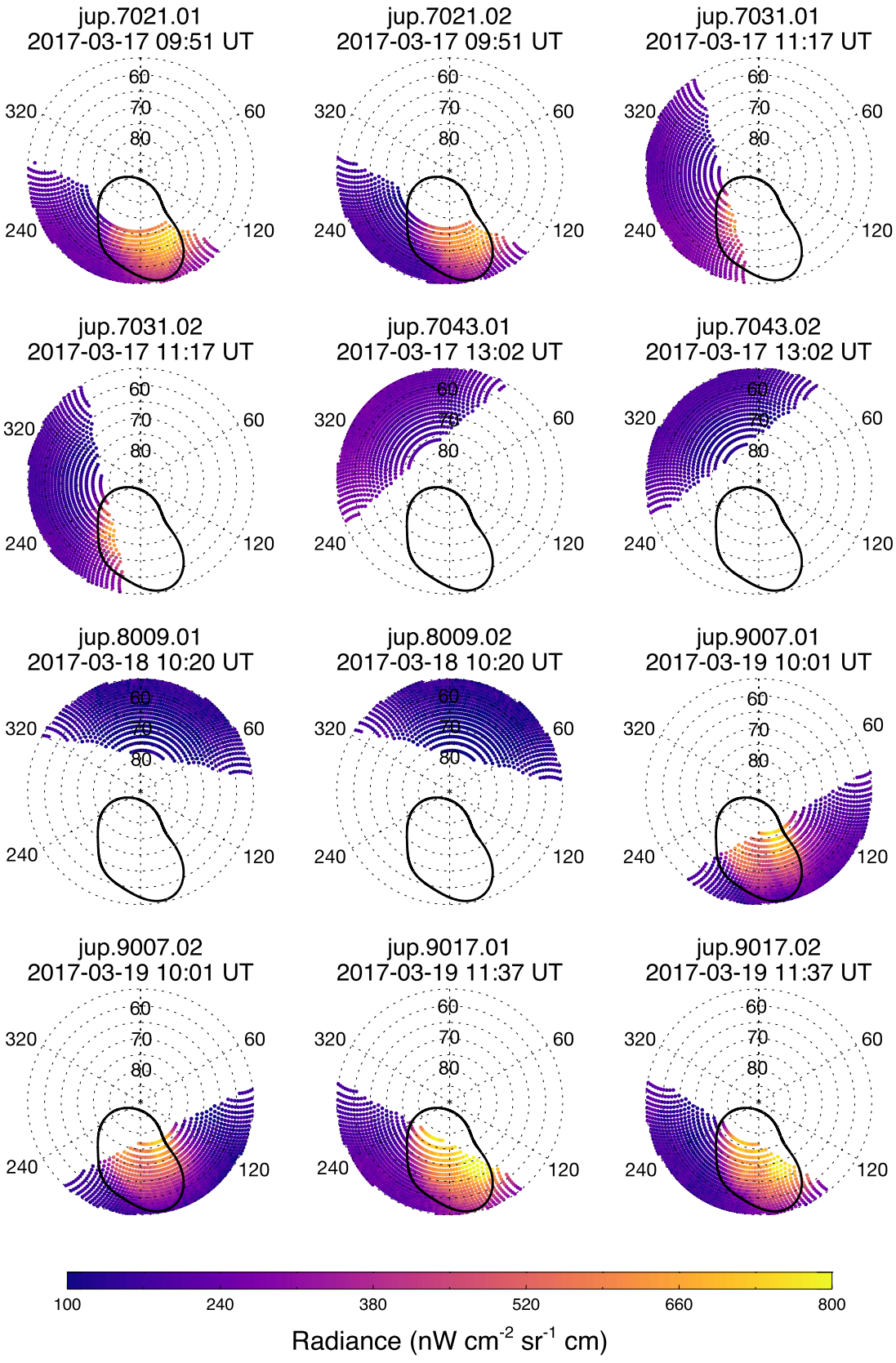

Figure B3. Individual TEXES scans of high northern latitudes. Each point represents a spectrum and is colored according to the mean radiance in all sampled C_2H_2 emission lines from 729.0 to 730.0 cm^{-1}. Scans are shown in chronological order from left to right and top to bottom. Solid black lines represent the statistical-mean position of the ultraviolet auroral ovals (Bonfond et al. 2017).

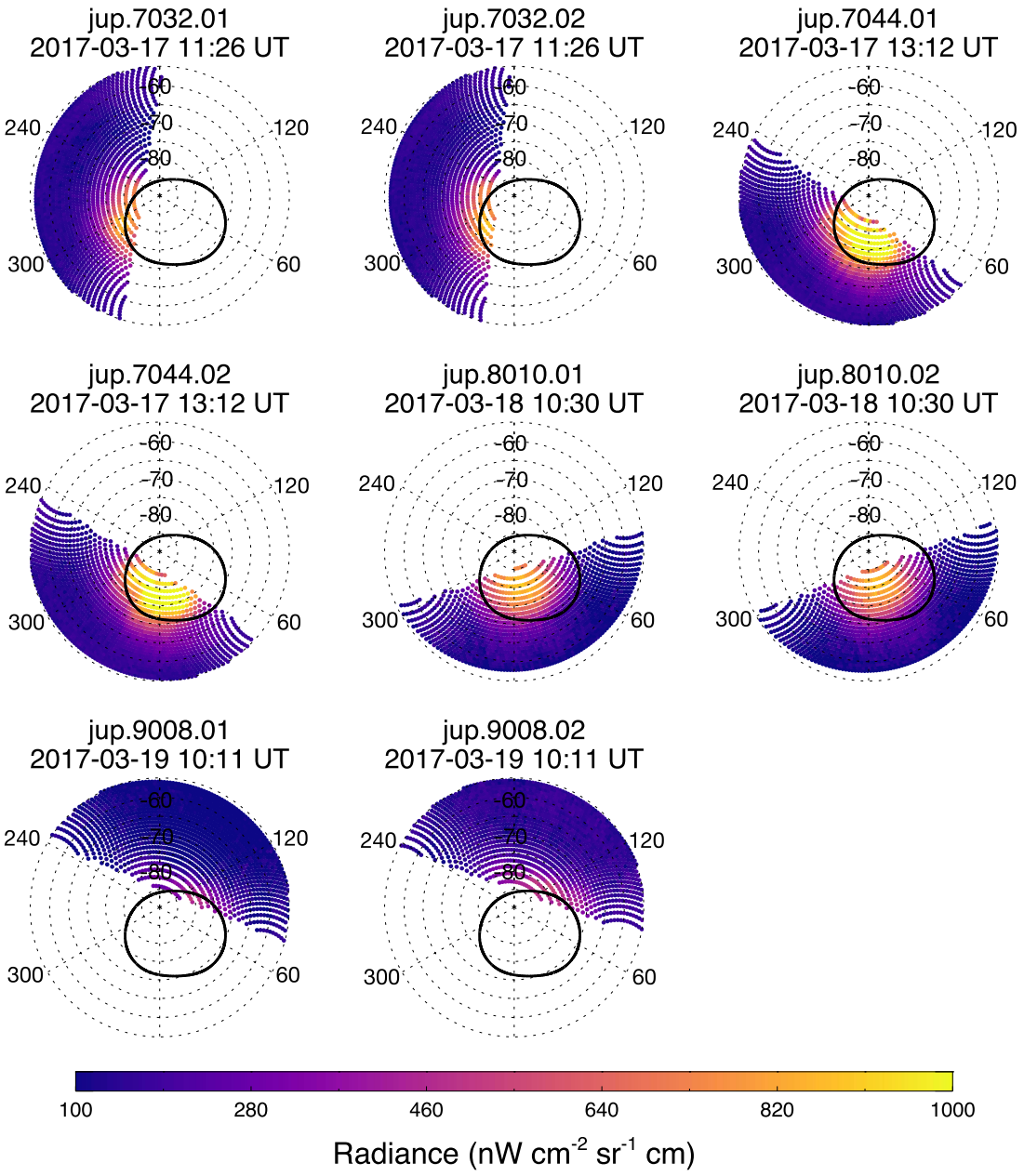

Figure B4. Same as Figure B3 but for observations of high southern latitudes.

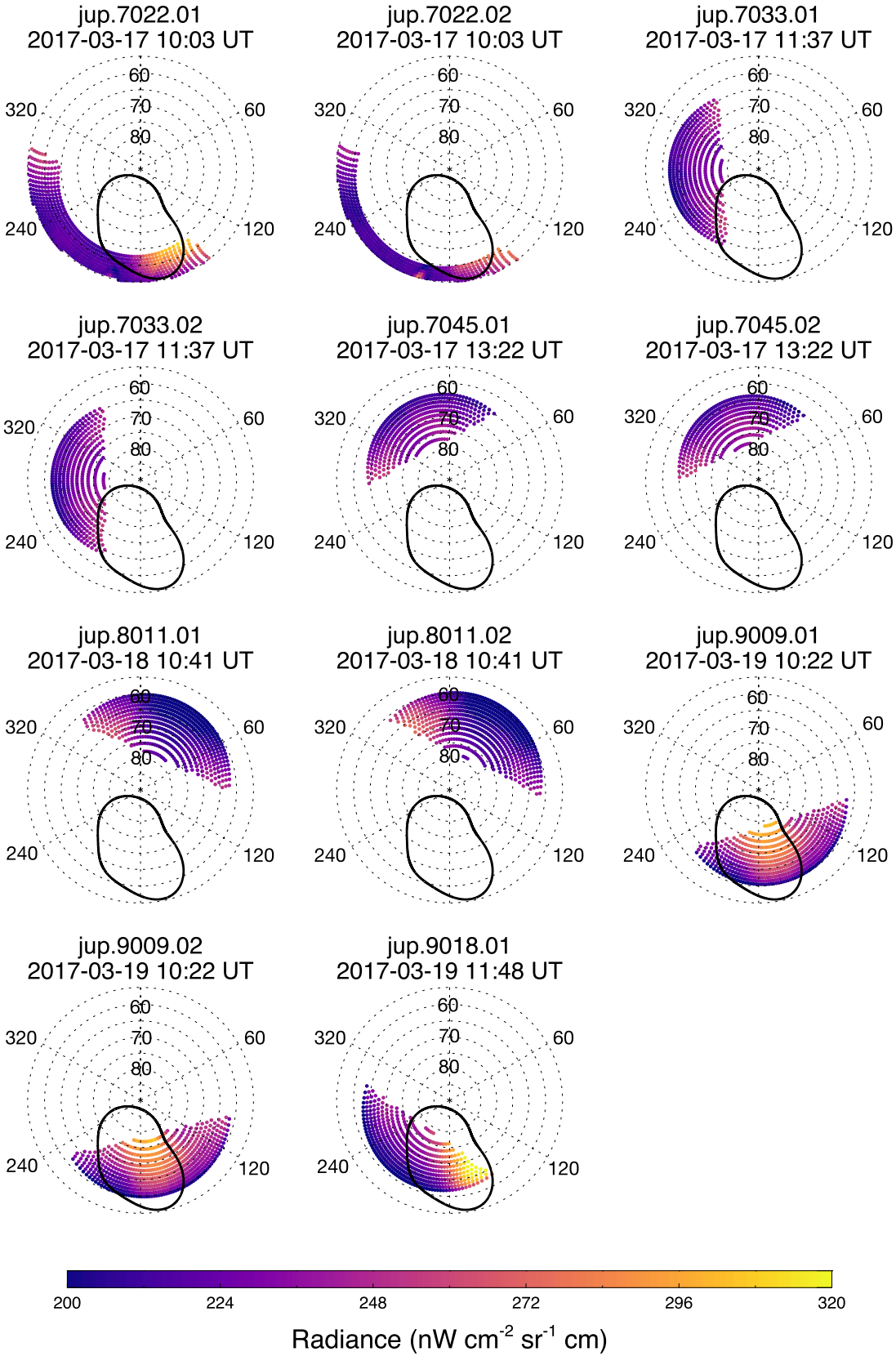

Figure B5. Individual TEXES scans of high northern latitudes. Each point represents a spectrum and is colored according to the mean radiance in all sampled C_2H_6 emission lines from 819.0 to 820.0 cm^{-1}. Scans are shown in chronological order from left to right and top to bottom. Solid black lines represent the statistical-mean position of the ultraviolet auroral ovals (Bonfond et al. 2017).

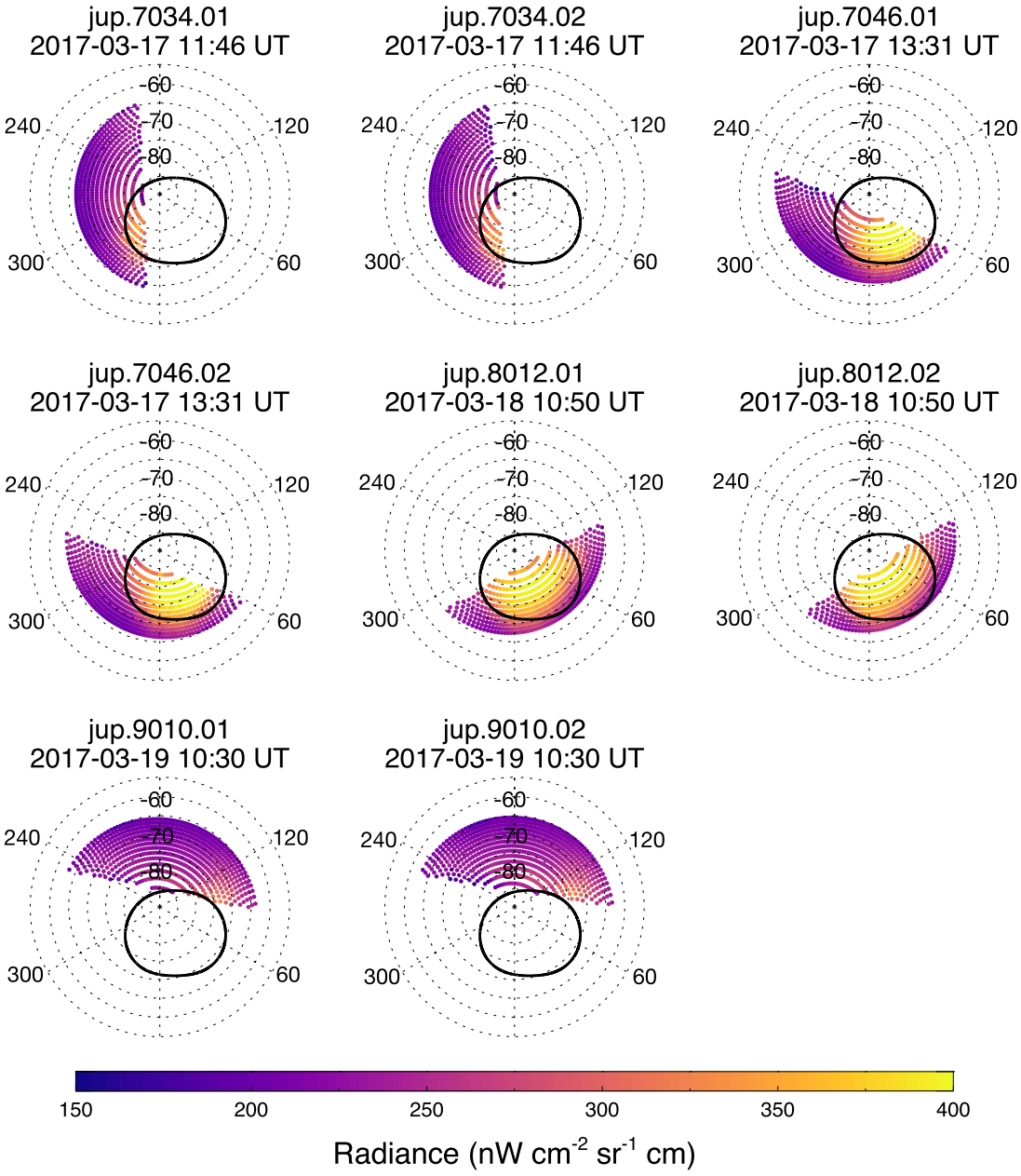

Figure B6. Same as Figure B5 but for observations of high southern latitudes.

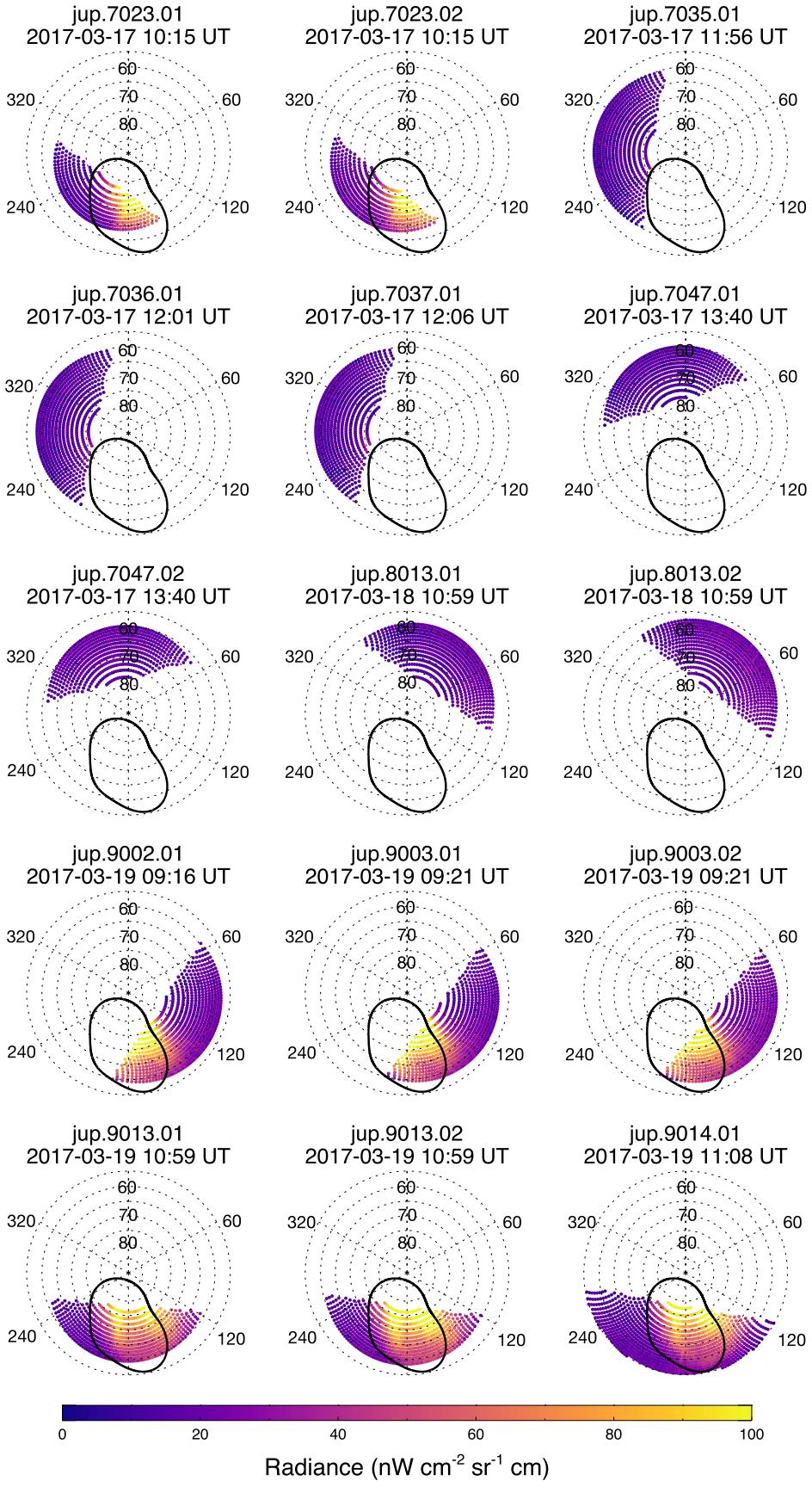

Figure B7. Individual TEXES scans of high northern latitudes. Each point represents a spectrum and is colored according to the mean radiance in all sampled C_2H_4 emission lines from 949.0 to 950.0 cm^{-1} Scans are shown in chronological order from left to right and top to bottom. Solid black lines represent the statistical-mean position of the ultraviolet auroral ovals (Bonfond et al. 2017).

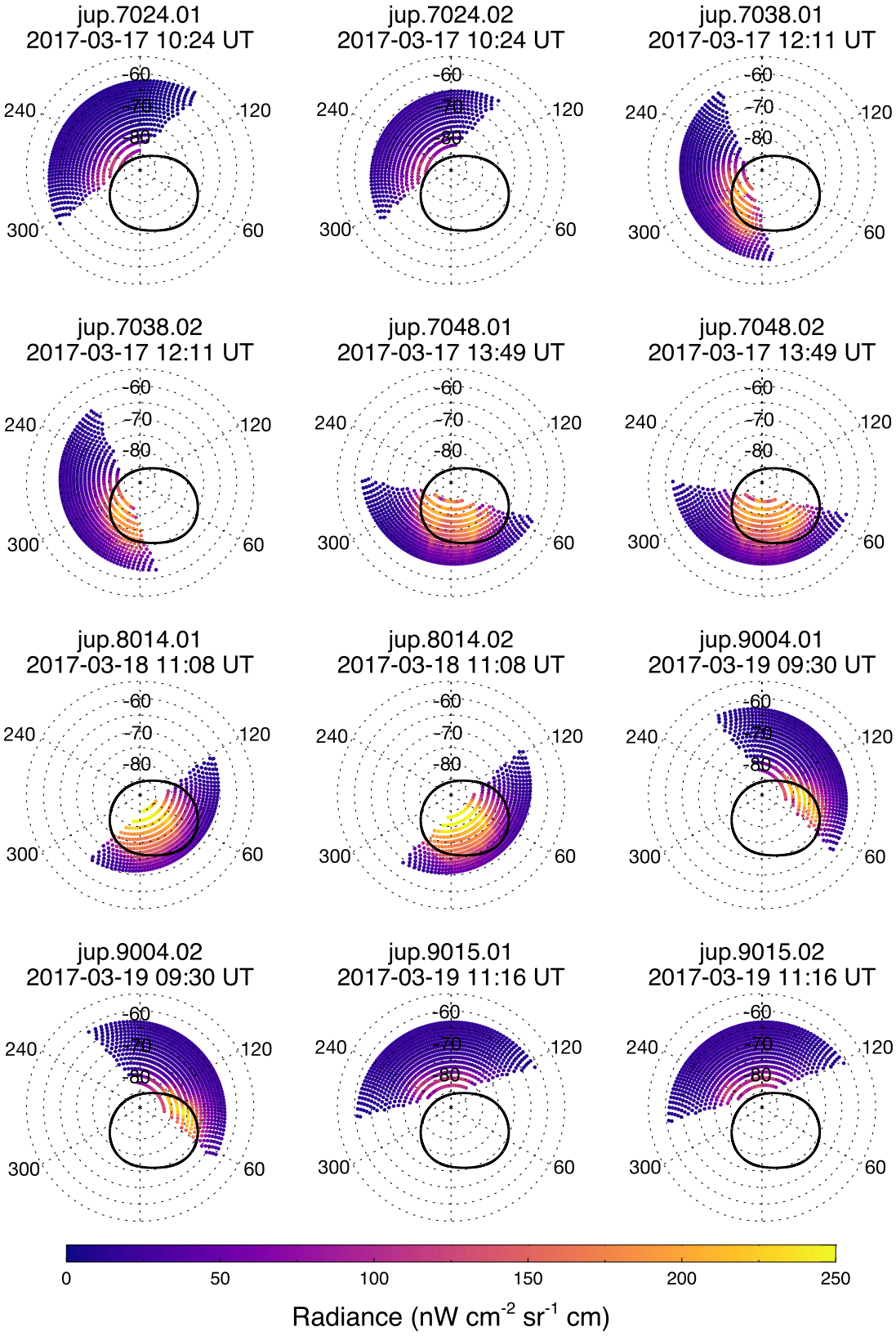

Figure B8. Same as Figure B7 but for observations of high southern latitudes.

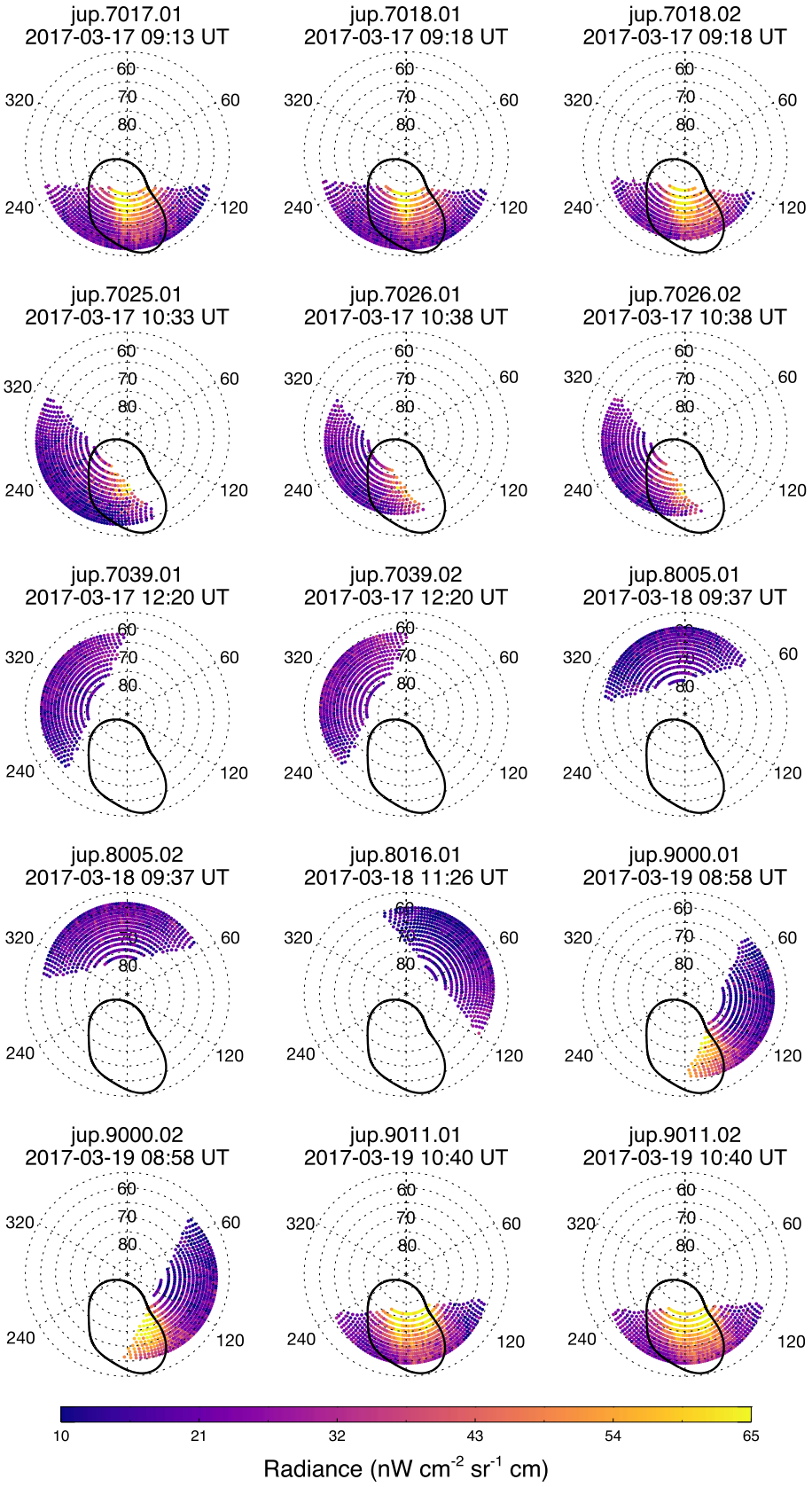

Figure B9. Individual TEXES scans of high northern latitudes. Each point represents a spectrum and is colored according to the mean radiance in all sampled CH_4 emission lines from 1245.20 to 1250.03 cm^{-1}. Scans are shown in chronological order from left to right and top to bottom. Solid black lines represent the statistical-mean position of the ultraviolet auroral ovals (Bonfond et al. 2017).

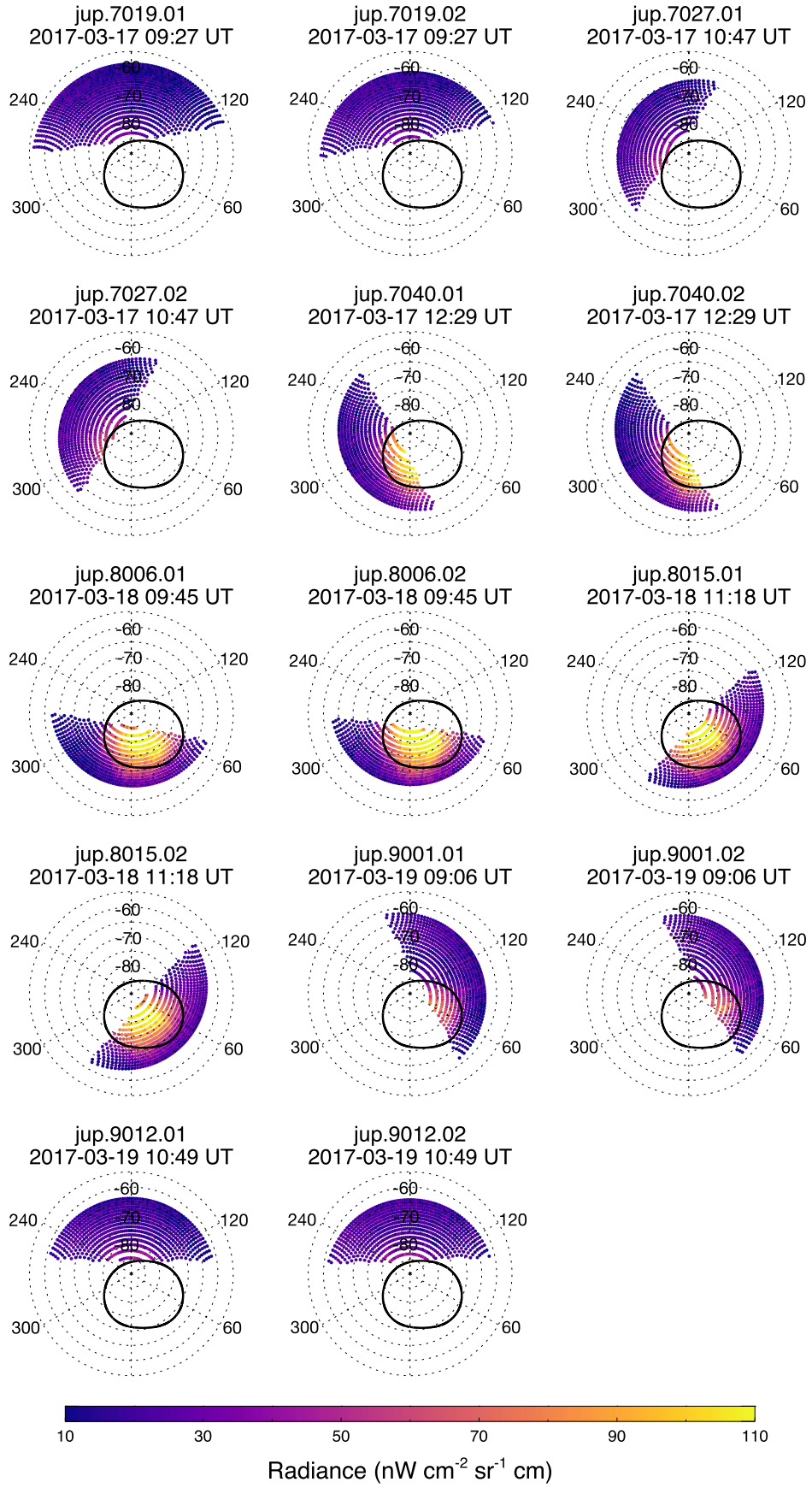

Figure B10. Same as Figure B9 but for observations of high southern latitudes.

Appendix C
C_2H_4 Retrieval Artifacts

Figure C1 shows example retrievals of temperature and C_2H_4 at two neighboring locations, where the retrieval places the enhancement of C_2H_4 with respect to a priori at different altitudes. Our interpretation is that a subset of retrievals converge on a secondary χ^2 minimum, corresponding to a poorer fitting, lower-stratospheric C_2H_4 enhancement, and a subset converge on a primary χ^2 minimum, corresponding to an upper stratospheric enhancement with an improved fit. As shown in Figure C2, reducing the uncertainty on the a priori C_2H_4 profile at deeper pressures ensures that retrievals converge on a better-fitting upper-stratospheric enhancement. See Section 5.1 of the main text for further details.

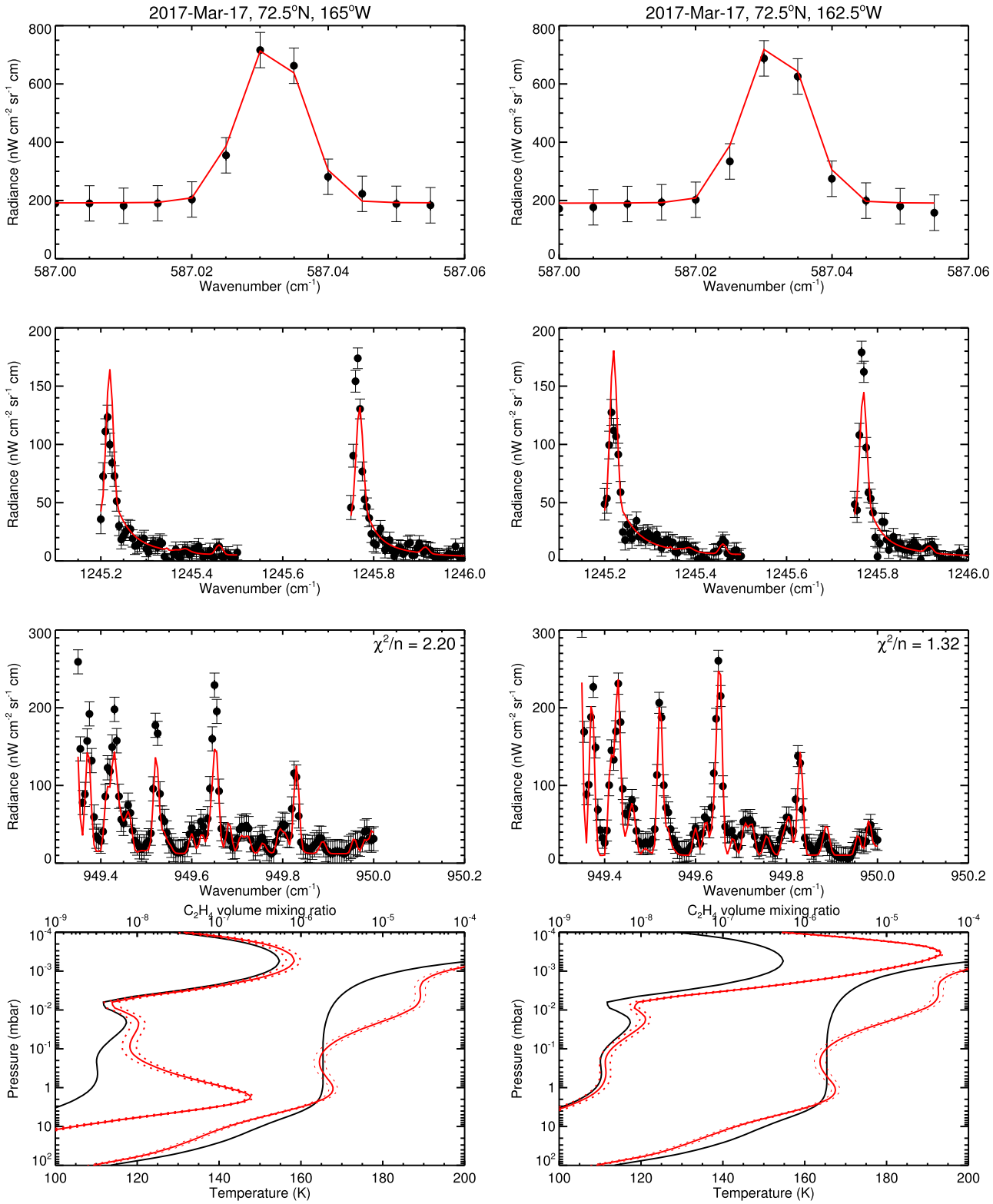

Figure C1. Example retrievals of temperature and C_2H_4 at 72.°5N, 165°W (left column) and 162.°5W (right column), where the retrieval places the enhancement of C_2H_4 with respect to a priori at different altitudes. The first and second rows compare observed and modeled spectra at 587 and 1248 cm^{-1}, respectively, from which the temperature profile is retrieved. The third row compares observed and modeled spectra at 950 cm^{-1} from which the C_2H_4 profile is retrieved. The bottom panel shows retrieved profiles (solid red, with dotted red lines showing the 1σ uncertainty) of the temperature, according to the lower axis, and C_2H_4, according to the upper axis. Solid black lines mark the a priori profiles.

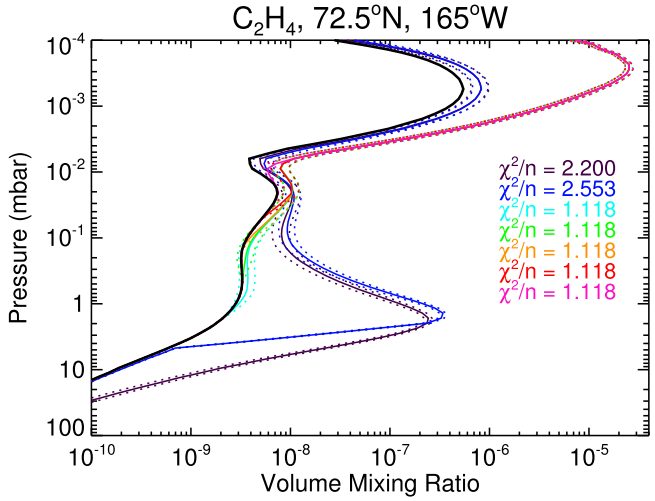

Figure C2. Retrievals of the vertical profile of C_2H_4 at 72°5N, 165°W using observations on 2017 March 19. The solid black line represents the initial guess or a priori profile. Solid and dotted lines represent retrieved profiles and uncertainties, respectively. Retrieved profiles are shown where the fractional uncertainty is constant at all altitudes (purple) and where it is reduced to 1% abundances at pressures higher than 3 (blue), 1 (cyan), 0.3 (green), 0.1 (orange), 0.03 (red), and 0.01 mbar (pink). The corresponding reduced χ^2/n values are shown in the legend.

ORCID iDs

James A. Sinclair https://orcid.org/0000-0001-5374-4028
Thomas K. Greathouse https://orcid.org/0000-0001-6613-5731
Rohini S. Giles https://orcid.org/0000-0002-7665-6562
John Lacy https://orcid.org/0000-0001-6783-2328
Julianne Moses https://orcid.org/0000-0002-8837-0035
Vincent Hue https://orcid.org/0000-0001-9275-0156
Denis Grodent https://orcid.org/0000-0002-9938-4707
Bertrand Bonfond https://orcid.org/0000-0002-2514-0187
Chihiro Tao https://orcid.org/0000-0001-8817-0589
Thibault Cavalié https://orcid.org/0000-0002-0649-1192
Emma K. Dahl https://orcid.org/0000-0003-2985-1514
Glenn S. Orton https://orcid.org/0000-0001-7871-2823
Leigh N. Fletcher https://orcid.org/0000-0001-5834-9588
Patrick G. J. Irwin https://orcid.org/0000-0002-6772-384X

References

Achilleos, N., Miller, S., Prangé, R., Millward, G., & Dougherty, M. 2001, NJPh, 3, 3.1
Acton, C. H. 1996, P&SS, 44, 65
Appleby, J. F. 1990, Icar, 85, 355
Badman, S. V., Branduardi-Raymont, G., Galand, M., et al. 2015, SSRv, 187, 99
Blain, D., Fouchet, T., Greathouse, T., et al. 2018, Icar, 314, 106
Bonfond, B., Grodent, D., Gérard, J.-C., et al. 2012, GeoRL, 39, L01105
Bonfond, B., Saur, J., Grodent, D., et al. 2017, JGRA, 122, 7985
Bonfond, B., Yao, Z., & Grodent, D. 2020, JGRA, 125, e28152
Bougher, S. W., Waite, J. H., Majeed, T., & Gladstone, G. R. 2005, JGRE, 110, E04008
Caldwell, J., Gillett, F. C., & Tokunaga, A. T. 1980, Icar, 44, 667
Cavalié, T., Benmahi, B., Hue, V., et al. 2021, A&A, 647, L8
Clarke, J. T., Nichols, J., Gérard, J. C., et al. 2009, JGRA, 114, A05210
Cowley, S. W. H., Bunce, E. J., Stallard, T. S., & Miller, S. 2003, GeoRL, 30, 1220
Delamere, P. A., & Bagenal, F. 2010, JGRA, 115, A10201
Drossart, P., Bezard, B., Atreya, S. K., et al. 1993, JGR, 98, 18803
Dunn, W. R., Branduardi-Raymont, G., Ray, L. C., et al. 2017, NatAs, 1, 758
Flasar, F. M., Kunde, V. G., Achterberg, R. K., et al. 2004, Natur, 427, 132
Fletcher, L. N., Greathouse, T. K., Orton, G. S., et al. 2016, Icar, 278, 128
Fletcher, L. N., Orton, G. S., Greathouse, T. K., et al. 2020, JGRE, 125, e2020JE006399
Fletcher, L. N., Orton, G. S., Sinclair, J. A., et al. 2018, NatCo, 9, 3564
Friedson, A. J., Wong, A.-S., & Yung, Y. L. 2002, Icar, 158, 389
Giles, R. S., Fletcher, L. N., & Irwin, P. G. J. 2017, Icar, 289, 254
Gladstone, G. R., Waite, J. H., Grodent, D., et al. 2002, Natur, 415, 1000
Greathouse, T., Gladstone, R., Versteeg, M., et al. 2021, JGRE, 126, e06954
Grodent, D. 2015, SSRv, 187, 23
Grodent, D., Bonfond, B., Yao, Z., et al. 2018, JGRA, 123, 3299
Grodent, D., Waite, J. H., Jr., & Gérard, J.-C. 2001, JGR, 106, 12933
Gustin, J., Grodent, D., Ray, L. C., et al. 2016, Icar, 268, 215
Hill, T. W. 2001, JGR, 106, 8101
Houston, S. J., Cravens, T. E., Schultz, D. R., et al. 2020, JGRA, 125, e27007
Hue, V., Greathouse, T. K., Gladstone, G. R., et al. 2021, JGRA, 126, e28971
Hue, V., Hersant, F., Cavalié, T., Dobrijevic, M., & Sinclair, J. A. 2018, Icar, 307, 106
Irwin, P. G. J., Teanby, N. A., de Kok, R., et al. 2008, JQSRT, 109, 1136
Johnson, R. E., Melin, H., Stallard, T. S., et al. 2018, JGRA, 123, 5990
Johnson, R. E., Stallard, T. S., Melin, H., Nichols, J. D., & Cowley, S. W. H. 2017, JGRA, 122, 7599
Kataza, H., Okamoto, Y., Takubo, S., et al. 2000, Proc. SPIE, 4008, 1144
Kim, S. J., Caldwell, J., Rivolo, A. R., Wagener, R., & Orton, G. S. 1985, Icar, 64, 233
Kimura, T., Hiraki, Y., Tao, C., et al. 2018, JGRA, 123, 1885
Kita, H., Kimura, T., Tao, C., et al. 2016, GeoRL, 43, 6790
Kostiuk, T., Livengood, T. A., Hewagama, T. H., et al. 2016, AGUFM, P33C–2155
Kostiuk, T., Romani, P., Espenak, F., & Livengood, T. A. 1993, JGR, 98, 18823
Kotsiaros, S., Connerney, J. E. P., Clark, G., et al. 2019, NatAs, 3, 904
Lacis, A. A., & Oinas, V. 1991, JGR, 96, 9027
Lacy, J. H., Richter, M. J., Greathouse, T. K., Jaffe, D. T., & Zhu, Q. 2002, PASP, 114, 153
Lellouch, E., Bézard, B., Fouchet, T., et al. 2001, A&A, 370, 610
Livengood, T. A., Kostiuk, T., & Espenak, F. 1993, JGR, 98, 18813
López-Puertas, M., & Taylor, F. 2001, Non-LTE Radiative Transfer in the Atmosphere, Series on Atmospheric, Oceanic and Planetary Physics (Singapore: World Scientific)
Lord, S. 1992, ATRANS: NASA Technical Memorandum 103957, https://atran.arc.nasa.gov
Masters, A., Dunn, W. R., Stallard, T. S., Manners, H., & Stawarz, J. 2021, JGRA, 126, e29544
Melin, H., Fletcher, L. N., Donnelly, P. T., et al. 2018, Icar, 305, 301
Moore, L., O'Donoghue, J., Melin, H., et al. 2017, GeoRL, 44, 4513
Mori, K., Hailey, C., Bridges, G., et al. 2022, NatAs, 6, 442
Moses, J. I., Armstrong, E. S., Fletcher, L. N., et al. 2015, Icar, 261, 149
Moses, J. I., Fouchet, T., Bézard, B., et al. 2005, JGRE, 110, E08001
Moses, J. I., & Poppe, A. R. 2017, Icar, 297, 33
Nichols, J. D., Badman, S. V., Bagenal, F., et al. 2017, GeoRL, 44, 7643
Nixon, C. A., Achterberg, R. K., Conrath, B. J., et al. 2007, Icar, 188, 47
O'Donoghue, J., Moore, L., Bhakyapaibul, T., et al. 2021, Natur, 596, 54
Ozak, N., Cravens, T. E., & Schultz, D. R. 2013, GeoRL, 40, 4144
Pan, D.-X., Yao, Z.-H., Manners, H., et al. 2021, GeoRL, 48, e91579
Press, W. H., Teukolsky, S. A., Vetterling, W. T., & Flannery, B. P. 1992, Numerical Recipes in FORTRAN. The Art of Scientific Computing (Cambridge: Cambridge Univ. Press)
Saur, J., Janser, S., Schreiner, A., et al. 2018, JGRA, 123, 9560
Seiff, A., Kirk, D. B., Knight, T. C. D., et al. 1998, JGR, 103, 22857
Sinclair, J., Orton, G., Greathouse, T., et al. 2018, EPSC, 12, EPSC2018–463
Sinclair, J. A., Greathouse, T. K., Giles, R. S., et al. 2020, PSJ, 1, 85
Sinclair, J. A., Moses, J. I., Hue, V., et al. 2019a, Icar, 328, 176
Sinclair, J. A., Orton, G. S., Fernandes, J., et al. 2019b, NatAs, 3, 607
Sinclair, J. A., Orton, G. S., Greathouse, T. K., et al. 2017a, Icar, 292, 182
Sinclair, J. A., Orton, G. S., Greathouse, T. K., et al. 2017b, GeoRL, 44, 5345
Sinclair, J. A., Orton, G. S., Greathouse, T. K., et al. 2018, Icar, 300, 305
Southwood, D. J., & Kivelson, M. G. 2001, JGR, 106, 6123
Tao, C., Kataoka, R., Fukunishi, H., Takahashi, Y., & Yokoyama, T. 2005, JGRA, 110, A11208
Thatcher, L. J., & Müller, H.-R. 2011, JGRA, 116, A12107
Wong, A.-S., Lee, A. Y. T., Yung, Y. L., & Ajello, J. M. 2000, ApJL, 534, L215
Wong, A.-S., Yung, Y. L., & Friedson, A. J. 2003, GeoRL, 30, 1447
Yao, Z. H., Bonfond, B., Grodent, D., et al. 2022, JGRA, 127, e2021JA029894
Yao, Z. H., Grodent, D., Kurth, W. S., et al. 2019, GeoRL, 46, 11,632
Yates, J., Achilleos, N., & Guio, P. 2014, P&SS, 91, 27
Yoshikawa, I., Suzuki, F., Hikida, R., et al. 2017, EP&S, 69, 110
Zhang, B., Delamere, P. A., Ma, X., et al. 2018, GeoRL, 45, 56
Zieger, B., & Hansen, K. C. 2008, JGRA, 113, A08107